J. Fluid Mech. (2008), *vol.* 613, *pp.* 171–203. © 2008 Cambridge University Press
doi:10.1017/S0022112008001900 Printed in the United Kingdom

Liquid interfaces in viscous straining flows: numerical studies of the selective withdrawal transition

MARKO KLEINE BERKENBUSCH[1], ITAI COHEN[2]
AND WENDY W. ZHANG[1]

[1]Department of Physics & James Franck Institute, The University of Chicago, 929 E. 57th Street, Chicago IL 60637, USA

[2]Physics Department, Cornell University, Ithaca, NY 14853, USA
mkb@uchicago.edu; ic64@cornell.edu; wzhang@uchicago.edu

(Received 18 October 2005 and in revised form 21 March 2008)

This paper presents a numerical analysis of the transition from selective withdrawal to viscous entrainment. In our model problem, an interface between two immiscible layers of equal viscosity is deformed by an axisymmetric withdrawal flow, which is driven by a point sink located some distance above the interface in the upper layer. We find that steady-state hump solutions, corresponding to selective withdrawal of liquid from the upper layer, cease to exist above a threshold withdrawal flux, and that this transition corresponds to a saddle-node bifurcation for the hump solutions. Numerical results on the shape evolution of the steady-state interface are compared against previous experimental measurements. We find good agreement where the data overlap. However, the larger dynamic range of the numerical results allows us to show that the large increase in the curvature of the hump tip near transition is not consistent with an approach towards a power-law cusp shape, an interpretation previously suggested from inspection of the experimental measurements alone. Instead, the large increase in the curvature at the hump tip reflects a robust trend in the steady-state interface evolution. For large deflections, the hump height is proportional to the logarithm of the curvature at the hump tip; thus small changes in hump height correspond to large changes in the value of the hump curvature.

1. Introduction

Topological transitions of a fluid interface are a key step in many important and complex physical processes. Simple examples include the formation and coalescence of droplets where local stresses typically determine the fluid flows near the transition. Here, we examine a different scenario where the topological transition in the interface shape is driven by a large-scale steady-state flow. Figure 1 depicts the experiment which inspired our numerical study. A deep layer of viscous silicone oil overlays a second immiscible layer, comprised of a mixture of water and glycerin (Cohen & Nagel 2002). Steady-state large-scale flows are created in the two fluid layers by withdrawing liquid through a tube placed in the upper layer and replacing the same amount of liquid into the upper layer at locations far away from the point of withdrawal. The rate of fluid withdrawal $\tilde{Q}$ dramatically affects the shape of the steady-state interface. When $\tilde{Q}$ is below a threshold value $\tilde{Q}_c$, the steady-state interface forms a hump. The lower-layer flow has the form of a toroidal recirculation, with a stagnation point at

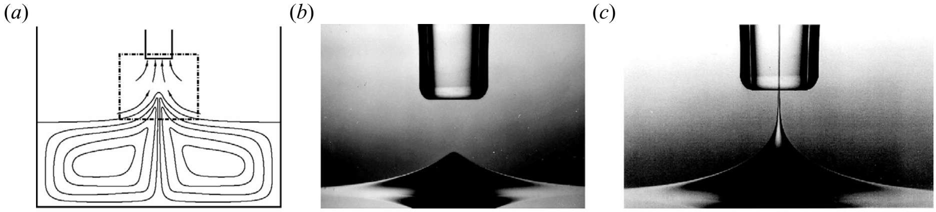

FIGURE 1. (*a*) Schematic of experiment. Liquid is withdrawn at a prescribed volume flux $\tilde{Q}$ through a tube inserted into the top layer and replenished at the same rate. The top layer is a viscous silicone oil. The bottom layer is a mixture of water and glycerin. The two layers have comparable viscosities. The flow rates are small so that viscous effects are significant in both layers. The tube diameter is 1.6 mm. (*b*) Selective withdrawal regime: below $\tilde{Q}_c$, a steady-state hump forms on the interface. (*c*) Viscous entrainment regime: above $\tilde{Q}_c$, a steady-state spout forms. Photographs courtesy of Cohen & Nagel (2002).

the tip of the hump. Since only liquid in the upper layer is withdrawn into the tube, this is known as the selective withdrawal regime. When the withdrawal flux $\tilde{Q}$ is larger than $\tilde{Q}_c$, the flows and the interface remain steady, but the interface attains a different topology. The steady-state interface is now ‘open’ and has the shape of a spout which extends smoothly into the tube. Since liquid is now withdrawn from both layers, this is known as the viscous entrainment regime. The large-scale toroidal recirculation in the lower layer is weakly perturbed by the onset of entrainment. The stagnation point moves slightly downwards, from the hump tip to the interior.

Analogous transitions from selective withdrawal to entrainment occur in many industrial and physical processes. Some examples on large length scales include the intrusion of water into an oil reservoir during the last stages of petroleum recovery (Renardy & Joseph 1985; Renardy & Renardy 1985), water-coning in sandy beds (Forbes, Hocking & Wotherspoon 2004), the formation of long-lived plumes by thermal convection in the Earth’s mantle (Davaille 1999; Jellinek & Manga 2002) and pollution recovery on lakes and oceans (Imberger & Hamblin 1982). On small length scales, the bursting of a liquid drop in a steady straining flow (Taylor 1934; Rallison & Acrivos 1978; Grace 1982; Stone 1994), the deposition of a thin trailing tendril by a drop sliding down an incline (Limat & Stone 2004) and the formation of thin cylindrical tendrils and droplets in micro-fluidic devices using axisymmetric flow-focusing (Anna, Bontourx & Stone 2003; Link *et al.* 2004; Lorenceau *et al.* 2005; Utada *et al.* 2005) all involve topological transition of steady-state interfaces.

In the selective withdrawal experiments, the curvature at the hump tip increases significantly as the transition is approached from below (Cohen & Nagel 2002; Cohen 2004). Measurements of the hump height and curvature evolution near the transition suggest the steady-state hump shape evolves towards a power-law cusp. In order to explain this apparent divergence, Cohen & Nagel made an analogy to recent works on topological transitions that correspond to the formation of a finite-time singularity in the governing equations. Some examples are the breakup of a liquid drop into two daughter drops (Eggers 1997; Cohen *et al.* 1999; Zhang & Lister 1999; Doshi *et al.* 2003), the coalescence of two drops into one (Oguz & Prosperetti 1990; Eggers, Lister & Stone 1999; Thoroddsen, Takehara & Etoh 2005), and the eruption of an electro-hydrodynamic spout under the sudden application of a large electric field (Oddershede & Nagel 2000). In all these situations, the topology change necessarily requires a divergence in the mean curvature at a point on the interface. As a result, the Laplace pressure due to surface tension, which is proportional to the mean curvature, diverges as well, thereby creating a singularity in the governing equations.

A number of questions are raised by this suggested analogy between the topological transition in viscous withdrawal and finite-time singularity formation. While the breakup of a liquid drop requires that the interface deforms continuously from a single connected shape to several disconnected shapes, and therefore requires the formation of a singular shape at breakup, the topological transition in this experiment deals with changes in the steady-state interface shape. The transition from selective withdrawal to viscous entrainment does not require that the hump shape evolve into the spout shape continuously as a function of the withdrawal flux $\tilde{Q}$. Generically, we would expect a discontinuous change in the steady-state shape across the selective withdrawal to viscous entrainment threshold.

Here we conduct a numerical analysis of a model withdrawal process in which the interface deformation is controlled solely by viscous stresses and surface tension. We focus on the selective withdrawal regime and analyse how the interface fails at the transition. In particular, we are interested in elucidating the factors that determine the final hump shape.

Another motivation for conducting this study is that experiments show the final hump shape is well correlated with the minimum spout thickness attained in the viscous entrainment regime (figure 1*c*). The viscous entrainment regime is important for a variety of practical applications. One such application entails taking advantage of viscous entrainment to encapsulate biological cells for transplant therapy (Cohen *et al.* 2001; Wyman *et al.* 2004). In this technique, the minimum spout size directly determines the minimum thickness of a protective polymer coating that can be applied to the cells. Consequently, a detailed understanding of this topological transition should help advance this technological application.

The rest of this paper is organized as follows. In § 2, we discuss related works and background materials. In § 3, we describe the model withdrawal process and its numerical formulation for a system in which the upper and lower fluid viscosities are equal. In § 4, we analyse solutions to the model and present results that identify the generic dynamics near the transition as a saddle-node bifurcation. We also find an atypical trend. As the interface deflection becomes large, the hump height couples logarithmically to the curvature at the hump tip. In § 5, we compare the numerical and experimental results and find excellent agreement between them. Moreover, we show that the logarithmic coupling between the hump height and the hump curvature can easily lead to a misinterpretation that the system approaches a steady-state singularity at the transition. A more detailed discussion of the distinction between the previous interpretation and our results is presented in § 6. Our findings indicate the transition from selective withdrawal to viscous entrainment involves a discontinuous change in the steady-state shape that has the structure of a saddle-node bifurcation. This discontinuity is effectively obscured in practice by the logarithmic coupling between the hump height and the hump curvature, which causes changes in the hump curvature to be far larger, and therefore more evident, than changes in the hump height as the transition is approached. These findings are summarized in greater detail in § 7.

2. Background

Many different realizations of flow-driven topological transitions have been investigated in previous works. Here, we review those studies that directly assess the ingredients necessary for a topological transition to take place and the appropriate ways of characterizing the evolution of the interface near such a transition.

2.1. *Viscous entrainment in geophysical flows*

A number of experimental and theoretical works have focused on the transition from selective withdrawal to viscous entrainment in stratified two-layer systems where surface-tension effects are assumed to be either negligible or weak. These studies were motivated by geophysical flows, in particular the emptying of a magma chamber during a volcanic explosion. Ivey & Blake (1985) investigated the threshold withdrawal flux $\tilde{Q}_c$ necessary for the onset of entrainment in miscible stratified layers. In a numerical study, Lister (1989) analysed the onset of entrainment in two liquid layers of equal viscosity and found that a finite value for $\tilde{Q}_c$ exists only if surface tension effects, however small, are included in the analysis. Its predictions for $\tilde{Q}_c$ as a function of the sink height have been compared against measurements by Cohen (2004). The studies by Ivey & Blake and Lister did not analyse the hump evolution near the transition, which is the focus of our work here.

2.2. *Two-dimensional analogues*

Air entrainment, such as occurs in high-speed coating (Simpkins & Kuck 2000) and in the impact of a jet of viscous liquid into a layer of the same viscous liquid (Lorenceau, Quéré & Eggers 2004) is often accompanied by the interface approaching a two-dimensional power-law cusp shape (Joseph *et al.* 1991). Jeong & Moffatt (1992) showed analytically that, in the idealized limit where air-flow effects are negligible, there is no transition from selective withdrawal to air entrainment. Instead, the interface shape approaches a steady-state singularity in the shape of a power-law cusp as the flow rate is increased towards infinity. Specifically, they showed via conformal mapping that the divergence of the curvature is proportional to $\exp(-Ca)$ where the capillary number Ca corresponds to a dimensionless withdrawal flux in the two-dimensional problem and measures the size of the viscous stresses, which sharpen the interface, against the smoothing effect of surface tension. More recent theoretical and experimental analyses (Eggers 2001; Lorenceau, Restagno & Quéré 2003) showed that, when air-flow effects are included, they perturb the idealized dynamics so that a transition to air entrainment occurs at finite flow rate. The approach towards a steady-state singularity is then cut off at a small length scale. Since the cutoff for air entrainment originates from viscous stresses associated with air flow, the cutoff length scale has a strong dependence on the viscosity contrast and increases as $(\mu_0/\mu)^{4/3}$, where μ_0 is the air viscosity.

2.3. *Selective withdrawal in three dimensions with viscous flow and surface tension*

In their studies of three-dimensional axisymmetric selective withdrawal, Cohen & Nagel (2002) used two liquids of comparable viscosities and measured $\tilde{h}$, the hump height, and $\tilde{\kappa}$, the mean curvature at the hump tip, as a function of the withdrawal flux $\tilde{Q}$. In a follow-up study, Cohen (2004) analysed the transition for different pairs of liquids. In particular, the viscosity ratio, defined as the viscosity of the liquid to be entrained divided by the viscosity of the entraining liquid, was varied from $O(1)$ to 10^{-3}. Analysis of the measurements show that, as the transition from selective withdrawal to viscous entrainment is approached from below, the steady-state hump curvature increases dramatically. Cohen & Nagel showed that this rate of increase can be fit to a power-law divergence. They also noted, however, that the hump never reaches a cusp shape. Instead, the final stage of the hump evolution is cut off by the transition. This behaviour led to the interpretation that a singular solution for the steady-state shape organizes the nearly continuous transition between the steady-state hump and spout shapes. The transition from a hump to a spout was observed when the radius of curvature at the hump tip was $O(50)\,\mu\text{m}$ or more. Moreover, the cutoff length scale shows little dependence on the viscosity contrast between the two layers. Consequently, axisymmetric viscous withdrawal in three dimensions differs strikingly from air entrainment in two dimensions, which shows a strong dependence of the cutoff length scale on the viscosity contrast.

2.4. *Viscous drainage*

An analogous, but not necessarily equivalent, topology change occurs in viscous drainage experiments, in which a viscous liquid exposed to air is placed in a container with an opening at the bottom surface and is allowed to drain out of the container owing to its own weight (Chaieb 2004; Courrech du Pont & Eggers 2006). As in the set-up by Cohen & Nagel, the drainage creates a large-scale toroidal recirculation whose viscous stresses deform the interface. Thus, the drainage experiment is geometrically equivalent to the Cohen & Nagel experiment, aside from being upside-down. One difference is that the layer depth of the withdrawn fluid changes with time in the drainage experiment, but remains constant in the set-up used by Cohen & Nagel. As the liquid drains out and the layer depth decreases below a critical value, a sharp cusp develops on the interface, a feature identified by Courrech du Pont & Eggers as a steady-state singularity. A further decrease in the layer depth causes the cusp to approach closer to the bottom surface and eventually intrude into the aperture through which the fluid is draining. Thus, no transition to viscous withdrawal was observed. Courrech du Pont & Eggers report that there is no transition from selective withdrawal to viscous entrainment during the entire drainage process. Moreover, the maximum curvature obtained in the drainage experiments, which corresponds to using two fluid layers with a viscosity contrast of 10^{-6}, are far larger than the maximum curvature measured by Cohen (2004) for two fluid layers with a viscosity contrast of 10^{-3}. The origin of these different outcomes is, at present, not understood.

2.5. *Viscous withdrawal in three dimensions with surface tension*

Motivated by the thin stable spout created in the viscous entrainment regime, Zhang (2004) analysed the transition in the reverse direction, from viscous entrainment to selective withdrawal. The analysis focuses on the regime where the viscosity of the fluid entrained is far smaller than the viscosity of the entraining liquid, and constrains the spout shape to be nearly cylindrical throughout. These simplifications allow the steady-state spout shape to be described via a long-wavelength model. Results for the model show that changing the boundary conditions on the interface, without changing the material parameters, can profoundly change the nature of the shape transition. For some boundary conditions, the steady-state interface deforms continuously with withdrawal flux from a spout to a hump across the transition. For other boundary conditions, the steady-state interface changes discontinuously at the transition. Thus, there appears to be a subtle interplay between the entraining flow and surface-tension effects. As a result, the transition is strongly influenced by constraints on the large-scale shape of the interface (Case & Nagel 2007).

2.6. *Emulsification*

Another extensively studied shape transition that has strong points of similarity with the selective withdrawal to viscous entrainment transition occurs when a single liquid drop is emulsified into several drops by an axisymmetric straining flow (Taylor 1934; Rallison & Acrivos 1978; Grace 1982; Stone 1994). In both situations, an imposed flow far from the interface induces flows near the interface between two viscous liquids. The steady-state interface is deformed at low flow rates and ‘broken’ at high flow rates. The crucial differences are that, for drop emulsification, there is no steady-state interface above the threshold flow rate. The drop is simply stretched out indefinitely by the flow. Also, even in the analogue of the selective withdrawal regime, when a steady-state shape exists for the drop, the flow dynamics are different because the flow inside the drop must assume a form satisfying global volume conservation. In contrast, for the two-layer withdrawal experiment, the layer depth is always much larger than the hump height. It is then reasonable to expect that the global volume constraint does not introduce a significant modification to the flow dynamics. We will show this expectation is indeed borne out by results from the numerics.

The viscosity contrast between the drop and surrounding fluid strongly affects the deformation-to-burst transition. When the drop is far less viscous than the surrounding liquid, the steady-state shape approaches a cusp shape as the burst transition is approached from below. In particular, the radius of curvature at the two elongated ends of the liquid drop is cut off on an exponentially small length scale (Acrivos & Lo 1978). Long-wavelength analysis of the extended drop shape in this regime also shows that the burst transition corresponds to a saddle-node bifurcation in the leading-order solution for the overall drop shape (Taylor 1964; Buckmaster 1973). When the drop viscosity is comparable with the surrounding liquid, the steady-state shape remains nearly spherical as the burst transition is approached. Numerics and phenomenological arguments have shown that the shape transition when the drop viscosity is equal to the surrounding liquid viscosity corresponds to a saddle-node bifurcation (Navot 1999; Blawzdziewicz, Cristini & Loewenberg 2002).

2.7. *Inviscid selective withdrawal*

Finally, we note that a similar flow-driven topological transition exists at high Reynolds number when water drains out of a filled bathtub (Sautreaux 1901; Lubin & Springer 1967). In practice, this process is typically accompanied by the formation of a vortex. More generally, withdrawal from two stratified layers of inviscid fluids is relevant for transport in water storage reservoirs, where often a layer of fresh water resides on top of a layer of salty water (Imberger & Hamblin 1982). Some of the results for the idealized problem of withdrawal from two layers of perfectly inviscid fluids (Tuck & Vanden-Broeck 1984; Vanden-Broeck & Keller 1987; Miloh & Tyvand 1993) suggest that, for the inviscid fluid system, the transition from selective withdrawal to full entrainment corresponds to the formation of a singular shape on the steady-state interface. This has motivated many recent theoretical and numerical studies, despite the fundamental difficulty that, without the small-scale smoothing provided by viscosity and/or surface tension in real life, the idealized problem is fundamentally ill-posed and can be approached only via careful limiting processes. For the same reason, direct comparison with experiments has also been difficult. For our study, the most relevant and suggestive results are that the two-dimensional withdrawal differs significantly from axisymmetric withdrawal in the inviscid studies (Forbes *et al.* 2004; Stokes, Hocking & Forbes 2005). Also, in both two-dimensional and axisymmetric withdrawal, whether selective withdrawal or full entrainment is realized can depend crucially on the initial conditions which determine transient evolution of the interface, instead of being solely determined by the boundary conditions (Hocking & Forbes 2001).

In sum, this brief review shows that studies of flow-driven topological transitions have produced a wealth of surprises. The wide range of behaviours observed indicates that apparently trivial differences in the exact experimental configurations can have a dramatic effect on the transition structure. On the other hand, the interface evolutions observed in these different situations share a number of common features, such as the existence of a topological transition at a finite flow rate, and the development of small-scale features on the interface near the transition. In order to make progress on the three-dimensional selective withdrawal problem, it is likely that experiments, simulations and theoretical calculations, all of which address the same flow geometry, will be required. This is one reason why our study focuses on devising and analysing a model withdrawal process that can be directly compared with the previous experiments of Cohen & Nagel.

3. Modelling selective withdrawal

This section describes our numerical model in the following order: we first identify the key parameters in the viscous withdrawal experiments by Cohen & Nagel and then describe an idealized withdrawal problem which retains these key features. A numerical formulation of the idealized problem, together with the approximations, is given in § 3.1. Section 3.2 gives details of the numerical implementation. The key approximations are that in our calculation the gradual flattening of the liquid interface owing to hydrostatic pressure on large length scales is approximated by a hard-cutoff length scale a. The gradual decay of the induced flow in the lower layer below the interface is approximated by a cutoff condition requiring that the pressure in the lower layer becomes uniform laterally across the liquid layer. Comparisons of results obtained using these approximations against those calculated using different boundary conditions (§ 4.3) and the experiment (§ 5) show that the simple numerical model reproduces the key features of the withdrawal process.

In the experiment, the height of the hump created is at most a few millimetres. The tube height S_p is comparable in size, ranging from 0.255 to 0.830 cm. The capillary length scale ℓ_γ, which characterizes the relative importance of surface tension and hydrostatic pressure, is about 0.55 cm. Deformations on length scales below $\ell_\gamma \equiv \sqrt{\gamma/\Delta\rho g}$ are stabilized by surface tension. Deformations on length scales above ℓ_γ are stabilized by hydrostatic pressure. All these length scales are much smaller than the dimensions of the liquid layer which is 12 cm deep and 30 cm in extent. Moreover, the experiments show that, provided that the tube height is sufficiently large, changes in the diameter of the tube have little effect on the interface deformation. This is the regime in which all the experimental data were taken. In this regime, the shape of the deformed interface is controlled solely by the capillary length scale ℓ_γ and the tube height S_p.

We use the observed hump height $\tilde{h}$ as the characteristic length scale, and $\tilde{Q}\tilde{h}/4\pi S_p^2$ a typical flow rate to define a Reynolds number $\rho\tilde{Q}/(\mu 4\pi S_p)$, where ρ is the density of the upper liquid, μ the viscosity of the upper layer. For typical experimental parameters, this ratio is approximately 0.2, indicating that inertial effects are small. We therefore assume $Re = 0$ in our analysis. The stress balance on the interface is therefore characterized by the capillary number,

$$Ca = \frac{\mu}{\gamma}\frac{\tilde{Q}}{4\pi S_p^2}, \tag{3.1}$$

a ratio of the strength of the viscous stresses exerted by the flow relative to the Laplace pressure due to surface tension. For a typical experiment, the transition from selective withdrawal to viscous entrainment corresponds to a threshold capillary number Ca_c in the range of 10^{-3}. Thus surface tension effects are strong even at the transition.

3.1. *Minimal model*

These results from the two-layer viscous withdrawal experiment motivate the following idealization. Since the container size is much larger than the characteristic length scale of the hump, the two immiscible liquid layers are taken as infinite in extent and in depth. We use a cylindrical coordinate system where $z=0$ corresponds to the height of the undisturbed flat interface and $r=0$ is the centreline of the withdrawal flow. To drive the withdrawal, we prescribe a sink flow

$$\boldsymbol{u}_{ext}(\boldsymbol{x}) = \frac{\tilde{Q}}{4\pi|\boldsymbol{x}_S - \boldsymbol{x}|^3}(\boldsymbol{x}_S - \boldsymbol{x}), \tag{3.2}$$

where $\boldsymbol{x}_S = \tilde{S}\boldsymbol{e}_z$ corresponds to a sink placed at height $\tilde{S}$ above the undisturbed interface and $\tilde{Q}$ is the strength of the point sink. This choice allows $\tilde{S}$ to be the only length scale imposed on the flow, consistent with the experimental observation that the hump shape depends primarily on the height of the withdrawal tube S_p and not on its diameter.

In the experiment, the tube height S_p is either comparable to, or smaller than, the capillary length scale ℓ_γ. This is a different situation from the geophysical flows examined by Lister (1989), for which $\ell_\gamma \ll S_p$. Because the capillary length scale is small relative to the characteristic length scale of geophysical flows, the interface deformation analysed by Lister levels out on a large length scale, one where hydrostatic pressure effects are more significant than surface tension effects. As a result, the force balance relevant for how the interface levels out is a balance between viscous stresses and hydrostatic pressure. In contrast, when $\ell_\gamma \gg S_p$, a limit not examined by Lister but more relevant for the selective withdrawal experiments, the interface deformation levels out on a length scale much shorter than the capillary length scale. As a result, the relevant force balance responsible for the flattening of the interface is that between surface tension and viscous stresses. This motivates us to treat the far-field condition differently from Lister's analysis. Instead of explicitly including the effect of hydrostatic pressure, we require that the interface has zero deflection at $r=a$. Physically, this pinning location a corresponds roughly to the capillary length scale ℓ_γ. In the calculation, the slope of the interface at $r=a$ is adjusted so that the pinning condition is satisfied at all flow rates. This introduces an error in the interface shape near $r=a$. This error is guaranteed to be small when the sink height $\tilde{S}$ is far smaller than a. It is small even when $\tilde{S}$ is comparable with a. In §4.3, we also show that, provided $\ell_\gamma > S_p$, including the hydrostatic pressure explicitly does not change our results.

Finally, since the interface evolution is observed to remain essentially the same even as the layer viscosities are made unequal, we assume the two liquids have exactly the same viscosity. These assumptions mean that the flow dynamics in the upper layer satisfies

$$\nabla \cdot \boldsymbol{\sigma}_1 = -\nabla p_1 + \mu \nabla^2 \boldsymbol{u}_1 = \boldsymbol{0}, \quad \nabla \cdot \boldsymbol{u}_1 = \boldsymbol{0}, \tag{3.3}$$

where $\boldsymbol{u}_1$ is the disturbance velocity field created in the upper layer owing to the presence of the liquid interface, p_1 is the pressure and $\boldsymbol{\sigma}_1$ is the stress field associated with the disturbance velocity field $\boldsymbol{u}_1$. Note that $\boldsymbol{u}_{ext}$ is a solution of Laplace's equation and therefore gives rise to a uniform and constant pressure distribution. The flow in the lower layer is created solely via the flow in the upper layer past the interface.

Therefore, $\boldsymbol{u}_2$, the disturbance velocity field in the lower layer, satisfies

$$\nabla \cdot \boldsymbol{\sigma}_2 = -\nabla p_2 + \mu \nabla^2 \boldsymbol{u}_2 = \mathbf{0}, \quad \nabla \cdot \boldsymbol{u}_2 = \mathbf{0}, \tag{3.4}$$

where p_2 is the pressure field in the lower layer and $\boldsymbol{\sigma}_2$ the fluid stress field in the lower layer.

Since the flow dynamics in both layers are described by the linear Stokes equations, we can represent the velocity field as an integral over a suitably defined closed surface, as discussed in earlier works and in textbooks on viscous flow (Lorentz 1907; Ladyzhenskaya 1963; Pozrikidis 1992). The key result of the boundary-integral formulation is that a Stokes velocity field $\boldsymbol{u}$ at a point $\boldsymbol{x}$ is given by an integral over any closed surface S enclosing $\boldsymbol{x}$. The surface integral has the form

$$\boldsymbol{u}(\boldsymbol{x}) = \int_S \boldsymbol{J}(\boldsymbol{r}) \cdot [\boldsymbol{n} \cdot \boldsymbol{\sigma}(\boldsymbol{y})] \, dS_y + \int_S \boldsymbol{n} \cdot \boldsymbol{K}(\boldsymbol{r}) \cdot \boldsymbol{u}(\boldsymbol{y}) \, dS_y, \tag{3.5}$$

where $\boldsymbol{y}$ is the point on the surface that is being integrated over and $\boldsymbol{n}$ is an outward-pointing surface normal. The tensors $\boldsymbol{J}$ and $\boldsymbol{K}$ are defined as:

$$\boldsymbol{J}(\boldsymbol{r}) = \frac{1}{8\pi\mu}\left(\frac{\mathbf{1}}{r} + \frac{\boldsymbol{rr}}{r^3}\right), \qquad \boldsymbol{K}(\boldsymbol{r}) = -\frac{3}{4\pi}\frac{\boldsymbol{rrr}}{r^5} \qquad (\boldsymbol{r} = \boldsymbol{x} - \boldsymbol{y}).$$

Physically, (3.5) indicates that the velocity at the interior point $\boldsymbol{x}$ can be expressed as a sum over two different kinds of contributions over the closed surface S. The first term on the right-hand side of (3.5) corresponds to the fluid stress exerted by flows past the enclosing surface. The second term describes contributions corresponding to flows into and along the closed surface S. If the point $\boldsymbol{x}$ lies outside the enclosed volume, the contributions over the closed surface cancel, so that the right-hand side of (3.5) sums to 0. A point on the closed surface S is a special case. When the closed surface S is continuous and smoothly varying, the velocity at $\boldsymbol{x}$ is simply an average of the contribution from S to $\boldsymbol{x}$ if it is in the exterior and the contribution from S to $\boldsymbol{x}$ if it is an interior point. As a result, the velocity for a point $\boldsymbol{x}$ on the surface S can be written as

$$\tfrac{1}{2}\boldsymbol{u}(\boldsymbol{x}) = \int_S \boldsymbol{J}(\boldsymbol{r}) \cdot [\boldsymbol{n} \cdot \boldsymbol{\sigma}(\boldsymbol{y})] \, dS_y + \int_S \boldsymbol{n} \cdot \boldsymbol{K}(\boldsymbol{r}) \cdot \boldsymbol{u}(\boldsymbol{y}) \, dS_y. \tag{3.6}$$

These results allow us to derive an integral equation for the time-evolution of the interface in our idealized withdrawal problem. We define the surface S_∞, which has the shape of a hemispherical shell with radius R_∞ such that R_∞ goes to infinity. We then divide the liquid interface into two portions, an inner portion, denoted by S_I, corresponding to the interface within a radial distance a of the origin, and an outer portion, denoted by S_O, corresponding to the rest of the interface. We then assume that the sink height is always much smaller than a so that contributions from the integral over S_O are small compared with contribution from S_I, and entirely discard the contribution from S_O. Our numerical results show that this is a reasonable procedure as long as the sink height $\tilde{S}$ is smaller than a (§4.2). In that regime, the hump height and radius of curvature are little influenced by the errors incurred in neglecting S_O. Starting from (3.5) and neglecting the contribution from S_O, the disturbance velocity $\boldsymbol{u}_1$ in the upper layer can be written as a sum of integrals over S_I and S_∞. Since $\boldsymbol{u}_1$ decays rapidly to $\mathbf{0}$ at infinity, the contributions from the integrals over the shell S_∞ approach 0 as R_∞ is taken to infinity, so that only the contribution

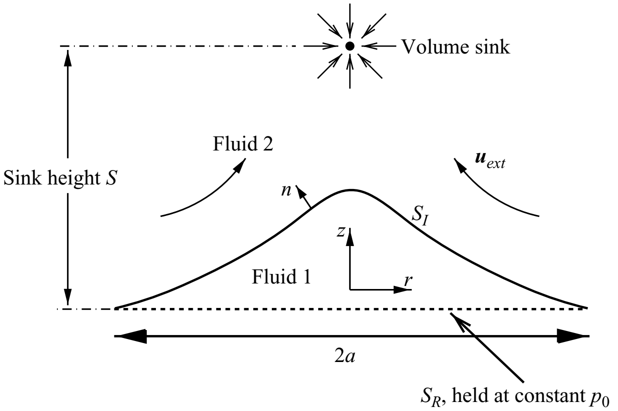

FIGURE 2. Simplified numerical model of selective withdrawal. The upper and lower liquid layers are separated by an interface S_I, constrained so that the deflection is non-zero only within a radius a. At a finite withdrawal flux, the surface S_R lies entirely within the lower layer.

from S_I to $\boldsymbol{u}_1$ remains. From (3.6), the velocity at a point on the interface is given by

$$\tfrac{1}{2}\boldsymbol{u}(\boldsymbol{x}) = \int_{S_I} \boldsymbol{J}\cdot(\boldsymbol{n}\cdot\sigma_1)\,\mathrm{d}S_y + \int_{S_I} \boldsymbol{n}\cdot\boldsymbol{K}\cdot\boldsymbol{u}_1\,\mathrm{d}S_y \quad \text{for } \boldsymbol{x}\in \boldsymbol{S}_I. \tag{3.7}$$

Finally, consider a point $\boldsymbol{x}$ on the surface S_R given by $z=0$, as depicted in figure 2. At a finite withdrawal flux, the interface is deflected away from the $z=0$ plane. As a result, points on S_R lie entirely inside the lower layer and therefore are not enclosed by the surface $S_I + S_\infty$; therefore the contribution from the surface integral over $S_I + S_\infty$ vanishes at a point $\boldsymbol{x}$ on S_R, or

$$\boldsymbol{0} = \int_{S_I} \boldsymbol{J}\cdot(\boldsymbol{n}\cdot\boldsymbol{\sigma}_1)\,\mathrm{d}S_y + \int_{S_I} \boldsymbol{n}\cdot\boldsymbol{K}\cdot\boldsymbol{u}_1\,\mathrm{d}S_y \quad \text{for } \boldsymbol{x}\in \boldsymbol{S}_R. \tag{3.8}$$

Next we consider the volume of liquid in the lower layer enclosed by the closed surface comprised of S_R and S_I. Again, starting with (3.6), we can write the velocity at a point $\boldsymbol{x}$ on either the liquid interface S_I or the surface S_R, here in after referred to as the ‘reservoir surface’, as

$$\tfrac{1}{2}\boldsymbol{u}(\boldsymbol{x}) = \int_{S_I} \boldsymbol{J}\cdot(\boldsymbol{n}\cdot\boldsymbol{\sigma}_2)\,\mathrm{d}S_y + \int_{S_I} \boldsymbol{n}\cdot\boldsymbol{K}\cdot\boldsymbol{u}_2\,\mathrm{d}S_y + \int_{S_R} \boldsymbol{J}\cdot(\boldsymbol{n}\cdot\boldsymbol{\sigma}_2)\,\mathrm{d}S_y$$
$$+ \int_{S_R} \boldsymbol{n}\cdot\boldsymbol{K}\cdot\boldsymbol{u}_2\,\mathrm{d}S_y \quad \text{for } \boldsymbol{x}\in S_I \text{ or } S_R, \tag{3.9}$$

where $\boldsymbol{n}$ is the outward pointing surface normal. As a result, for a point $\boldsymbol{x}$ on the liquid interface S_I, the surface integral over S_I in (3.9) has exactly the opposite sign to the surface integral over S_I in (3.7). Since the velocity is continuous across the interface, the two surface integrals involving the $\boldsymbol{K}$ tensor cancel exactly when the two equations, (3.9) and (3.7), for the velocity at a point $\boldsymbol{x}$ on the interface are added together. As a result, the velocity on the liquid interface can be re-written as

$$\boldsymbol{u}(\boldsymbol{x}) = \int_{S_I} \boldsymbol{J}\cdot[\boldsymbol{n}\cdot\boldsymbol{\sigma}]_-^+\,\mathrm{d}S_y + \int_{S_R} \boldsymbol{J}\cdot(\boldsymbol{n}\cdot\boldsymbol{\sigma}_2)\,\mathrm{d}S_y$$
$$+ \int_{S_R} \boldsymbol{n}\cdot\boldsymbol{K}\cdot\boldsymbol{u}_2\,\mathrm{d}S_y \quad \text{for } \boldsymbol{x}\in S_I, \tag{3.10}$$

where $[\boldsymbol{n}\cdot\boldsymbol{\sigma}]^+_- = \boldsymbol{n}\cdot\boldsymbol{\sigma}_1 - \boldsymbol{n}\cdot\boldsymbol{\sigma}_2$ denotes the jump in the normal stress across S_I owing to surface tension and is equal to $2\gamma\tilde{\kappa}\boldsymbol{n}$ where $\tilde{\kappa}$ is the mean surface curvature and $\boldsymbol{n}$ points outwards from S_I and S_R. Similarly, adding (3.8) and (3.9) yields an expression for the velocity at a point $\boldsymbol{x}$ on the reservoir surface S_R

$$\begin{aligned}\tfrac{1}{2}\boldsymbol{u}_2(\boldsymbol{x}) = &\int_{S_I} \boldsymbol{J}\cdot[\boldsymbol{n}\cdot\boldsymbol{\sigma}]^+_-\,\mathrm{d}S_y \\ &+ \int_{S_R} \boldsymbol{J}\cdot(\boldsymbol{n}\cdot\boldsymbol{\sigma}_2)\,\mathrm{d}S_y + \int_{S_R} \boldsymbol{n}\cdot\boldsymbol{K}\cdot\boldsymbol{u}_2\,\mathrm{d}S_y \quad \text{for } \boldsymbol{x}\in S_R. \end{aligned} \tag{3.11}$$

Equations (3.10) and (3.11) together provide an expression for the velocity on the liquid interface as a function of the interface shape, and $\boldsymbol{n}\cdot\boldsymbol{\sigma}_2|_{S_R}$, the stress exerted by flow in the lower layer on the reservoir surface S_R. In a full calculation, $\boldsymbol{n}\cdot\boldsymbol{\sigma}_2|_{S_R}$ must be obtained separately and then used in (3.10) and (3.11) to calculate the velocity on the liquid interface. Here, we simplify the calculation and prescribe the normal stress distribution on S_R. Specifically, we require that the normal stress is a spatially uniform pressure of size p_0, so that

$$\boldsymbol{n}\cdot\boldsymbol{\sigma}_2|_{S_R} = -p_0\boldsymbol{n}. \tag{3.12}$$

This choice of the stress condition (3.12) is motivated by the observation that, since the lower layer is taken to be infinitely deep, the stress distribution far from the interface must decay smoothly onto one that corresponds to a stagnant layer. This is simply a spatially uniform pressure field. By imposing this distribution at S_R, instead of a boundary condition far from the interface, we are essentially approximating the smooth decay that would be obtained in a deep lower layer as an abrupt cutoff at S_R. This is in the same spirit as approximating the effect of hydrostatic pressure by introducing a pinning length a for the interface and is just as effective in capturing the key features of the interface evolution. A more realistic simulation which includes a lower layer of finite depth, instead of imposing (3.12) at S_R yields essentially the same results (§ 4.3).

With these considerations in mind the disturbance velocity on the interface is given by

$$\begin{aligned}\boldsymbol{u}(\boldsymbol{x}) = &\int_{S_I} \boldsymbol{J}\cdot\boldsymbol{n}\,[\gamma 2\tilde{\kappa}]\,\mathrm{d}S_y \\ &+ \int_{S_R} \boldsymbol{J}\cdot(-p_0\boldsymbol{n})\,\mathrm{d}S_y + \int_{S_R} \boldsymbol{n}\cdot\boldsymbol{K}\cdot\boldsymbol{u}_2\,\mathrm{d}S_y \quad \text{for } \boldsymbol{x}\in S_I \end{aligned} \tag{3.13}$$

where the velocity on S_R required in order to evaluate the third surface integral in (3.13) can be found by solving the integral equation given by (3.11). The total velocity on the interface is a sum of the disturbance velocity and the imposed withdrawal flow. Therefore, to update the interface, we use the kinematic condition

$$\frac{\mathrm{d}\boldsymbol{x}}{\mathrm{d}t} = \boldsymbol{u}(\boldsymbol{x}) + \boldsymbol{u}_{ext} \quad \text{for } \boldsymbol{x}\in S_I. \tag{3.14}$$

To find a steady-state hump profile for a given withdrawal flux, we start with an initial guess and solve (3.11), (3.13) and (3.14) in succession until either a steady state is obtained or the interface deformation grows so large that the interface reaches the sink.

Finally, we non-dimensionalize the withdrawal problem via the following characteristic length, velocity and stress scales

$$\hat{\ell} = a, \qquad \hat{u} = \frac{\gamma}{\mu}, \qquad \hat{p} = \frac{\gamma}{a}. \tag{3.15}$$

The dimensionless withdrawal flux is then

$$Q = \frac{\mu \tilde{Q}/a^2}{\gamma}. \tag{3.16}$$

This dimensionless withdrawal flux is related to the capillary number Ca, (3.1), defined earlier for the withdrawal experiments via $Q = 4\pi Ca(S_p/a)^2$. In addition to the dimensionless flow rate Q, there are two other parameters, the pressure $p_0 = \tilde{p}_0/\hat{p}$ imposed on the reservoir surface and the dimensionless sink height $S = \tilde{S}/a$.

3.2. *Numerical implementation*

We use a C++ code to solve the governing integral equations (3.11), (3.13) and (3.14). Since the problem is axisymmetric, all the surfaces involved can be represented as effectively one-dimensional objects by their r- and z-coordinates in a cylindrical coordinate system. The liquid interface is parameterized by mesh points $r_j(s_j)$, and $z_j(s_j)$, where s_j denotes the arclength along the surface measured from the tip. The interface between mesh points is approximated by a cubic spline. This way, the curvature calculated for the Laplace pressure term varies continuously between mesh points. The distribution and number of points is adapted to the geometric shape of the surface. The algorithm we implemented chooses the density of points to be proportional to the mean curvature (in most runs $\Delta s = 0.05/\kappa$, where Δs is the arclength between two adjacent mesh points). In addition, we require that adjacent mesh points cannot be separated by Δs larger than a maximum value. For most runs, this value was chosen to be of the order of 1/20 in dimensionless units. Since the interface at $Q = 0$ is nearly flat, it is represented by 20 grid points. During a typical run, the number of mesh points on the interface is dynamically increased to about 60 in order to resolve a dimensionless tip curvature of approximately 75. Doubling the mesh resolutions yields no significant change in the results. The velocities between mesh points on the reservoir surface are interpolated linearly.

For most runs shown in this paper, p_0 was chosen to be 0.01. As described in §4.2, we also analysed the effect of changing p_0 and found the value of p_0 does not affect the steady-state evolution near transition in any significant way.

The azimuthal component of the boundary-integral equations is integrated analytically and the resulting elliptic integrals are evaluated numerically (see Lee & Leal 1982). The boundary integrals are evaluated using Gaussian quadratures. Singular parts of the integral are dealt with separately using finer subdivisions of the integration interval, and the resulting algebraic equations for the unknown velocities and stresses are solved by LU (lower and upper triangular matrix) decomposition.

The mesh points on the interface are advanced in time via explicit forward Euler time stepping. To ensure that the mesh points remain evenly distributed, only the normal component of the velocity is used to update the interface. The length of each time step is chosen to be proportional to the smallest mesh spacing. The validity of this approach was tested by doubling the time resolution for a given run and comparing to the original results. Generally, results obtained this way differed by less than 1%. We also experimented with an implicit backward Euler scheme, but the evaluation of the necessary Jacobian was prohibitively slow, and the results obtained by the two methods did not differ significantly.

The scheme for finding steady-state shapes and critical flow rates follows the experimental procedure: starting with a static configuration at zero flow rate, Q is increased in small steps and for each step the interface is allowed to relax into a steady-state shape. Steady-state is detected by observing that the modulus of the highest normal velocity on the interface, $\boldsymbol{u}_{max} \cdot \boldsymbol{n}$, falls below a certain threshold (10^{-3} in dimensionless velocity units in most cases; lower thresholds were tested without significantly changing the results). When u_{max} increases monotonically by a certain factor, we deduce that a steady-state hump shape ceases to exist. In this case, the interval between the last steady-state flow rate and the current flow rate is divided in half, creating nesting intervals containing the critical flow rate Q_c. This procedure stops when the size of the interval between Q values has decreased below the desired accuracy. To resolve the steady-state evolution near Q_c, we also choose Q values between those chosen from the bisection and solve for the steady-state interface shape at these values.

Since the successive increases in the imposed withdrawal flux Q become very small near Q_c and the initial velocity on the interface is proportional to the increment in Q, the velocity on the interface becomes small near Q_c regardless of whether the interface shape is stable. We therefore allow the interface to evolve for a longer interval in time before checking whether the u_{max} exceeds the threshold value when Q is close to Q_c. We have also compared our results against runs done with an even longer interval of waiting time to ensure that the simulation has converged onto the steady-state solution.

4. Results

Using the equations governing the model withdrawal problem described in § 3, we calculate numerical solutions for the interface evolution near the transition. Section 4.1 describes how the curvature κ and the hump height h scale with the withdrawal flux Q near the transition. This section also addresses the coupling between h and κ. Section 4.2 shows the same results are obtained for different p_0 and sink height S values. In § 4.3, we analyse different realizations of the withdrawal problem and show that a logarithmic coupling between the maximum hump curvature and hump height obtains in all cases. A comparison between the numerical results and the measurements is given in § 5.

4.1. *Interface evolution and transition*

Time-dependent simulations of (3.11), (3.13) and (3.14) show that steady-state solutions corresponding to hump shapes are found only below a threshold flow rate Q_c. Above Q_c, no hump solutions are found. Figure 3 shows a sequence of the calculated steady-state shapes for $S = 1$. At $Q = 0$, the static interface is a spherical cap shape determined by a balance of surface tension and reservoir pressure $p_0 = 0.2$. When the imposed withdrawal flux Q is small, the interface is weakly perturbed from the spherical cap shape. At larger Q, a broad hump develops on the interface. As Q approaches Q_c, the hump height increases slightly, but the hump curvature increases dramatically. Above Q_c, the interface develops a finger-like structure which lengthens over time and eventually reaches the sink (figure 3 inset). For all Q, the shape of the hump at its tip remains smooth, well-fit by a spherical cap with mean curvature κ. We identify the disappearance of a steady-state hump solution at Q_c in the numerical solutions with the hump-to-spout transition observed in the experiment.

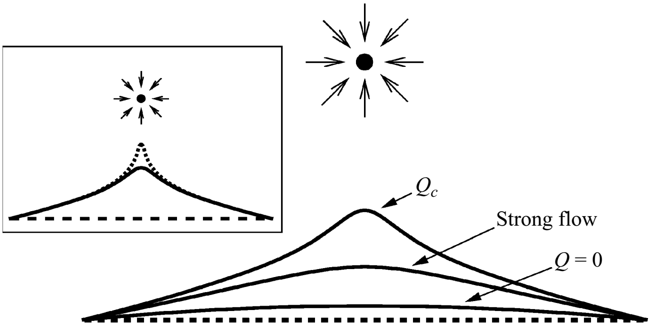

FIGURE 3. Steady-state interface shapes (solid lines) at different Q. For $Q=0$, the interface assumes a spherical cap shape for which the Laplace pressure balances the reservoir pressure p_0. As Q increases, the steady-state shape develops a hump towards the sink. The inset shows that, above the transition withdrawal flux Q_c, the unsteady interface (dashed line) develops a finger reaching towards the sink. Here, the dimensionless sink height $S \equiv \tilde{S}/a=1$ and the dimensionless reservoir pressure jump p_0 is 0.2.

In the rest of this subsection, we will analyse a typical set of results, obtained with dimensionless sink height $S=0.2$ and reservoir pressure p_0 set to 0.01. We can quantitatively characterize the interface evolution by plotting the hump height h and the mean curvature κ at the tip of the hump as functions of the withdrawal flux Q (figure 4). As Q approaches Q_c, the hump height saturates at h_c (figure 4*a*) and the curvature saturates at κ_c (figure 4*b*). The insets show that h and κ approach their saturation values as

$$\frac{h_c-h}{h_c} \propto \sqrt{\delta q}, \qquad \frac{\kappa_c-\kappa}{\kappa_c} \propto \sqrt{\delta q}, \qquad \delta q \equiv \frac{Q_c-Q}{Q_c}. \tag{4.1}$$

To obtain the best power-law fit, the h_c and Q_c values were adjusted slightly. The best fit is obtained when the values of h_c and Q_c were increased from the h and Q values corresponding to the final steady-state hump shape calculated by 0.03 % and 4×10^{-5} %, respectively. The κ_c value is adjusted by less than 0.001 % from the final hump curvature value obtained numerically. The same Q_c value is used in all the plots. All the adjustments are within the error bars of the simulation.

The observed square-root dependence of h_c-h and $\kappa_c-\kappa$ suggests that the transition from selective withdrawal to viscous entrainment occurs via a collision at Q_c of two steady-state hump solutions, one stable and one unstable. In other words, the transition from selective withdrawal to viscous withdrawal has the structure of a saddle-node bifurcation. Typically, saddle-node bifurcations are associated with solutions that remain smooth at the bifurcation point. Therefore, the observed square-root scaling suggests that the final evolution of the interface as the transition is approached is not organized by an approach towards a singular steady-state shape.

The saddle-node structure of the transition can be rationalized by considering the flow in the upper layer. It converges along the centreline and therefore speeds up away from the tip of the hump. Since the hump solution is realized in a time-dependent simulation and also observed in the experiment, it is linearly stable. We therefore expect that small upwards, perturbations of the hump tip simply decay downwards as the hump shape relaxes towards the steady-state solution over time. However, if the upwards perturbation is very large, so that the perturbed hump tip now lies very close to the sink, then surface tension effects will be too weak to pull the perturbed interface downwards. Instead, the hump tip will be drawn into the sink.

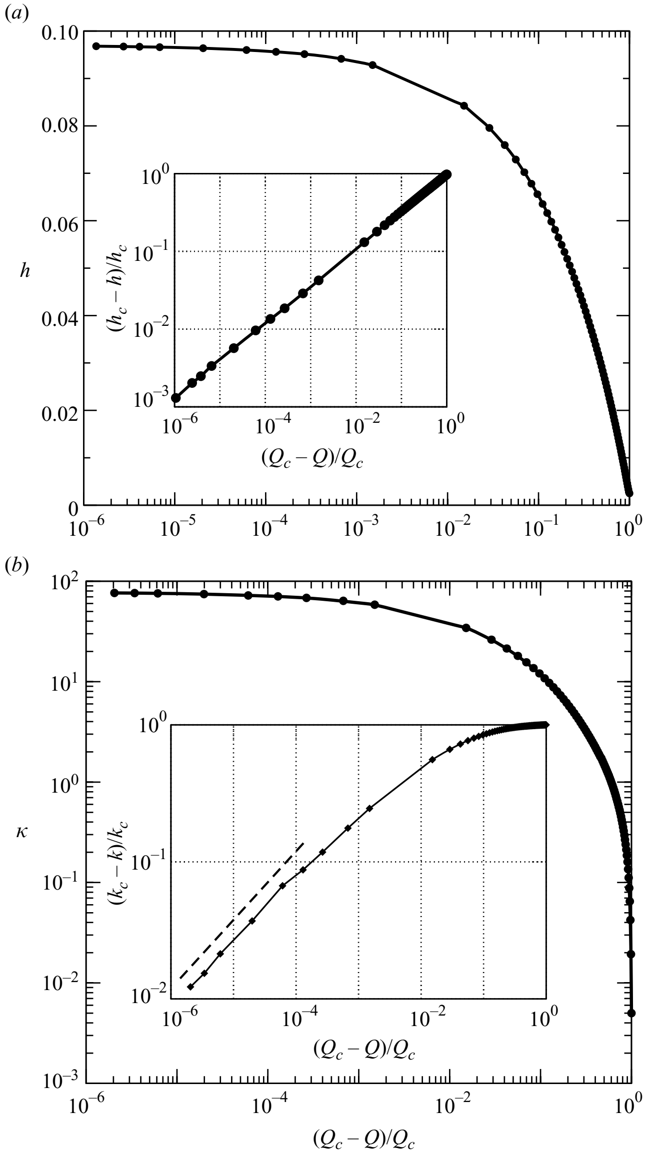

FIGURE 4. Evolution of the calculated steady-state hump shape with withdrawal flux Q. The model parameters are $S = 0.2$ and $p_0 = 0.01$. We find the transition flow rate to be $Q_c = 0.0731094$. Using fits to the numerical data at this flow rate, we find that the hump height $h_c = 0.09680$ and the hump curvature $\kappa_c = 76.453$. (*a*) Hump height h *vs.* $Q_c - Q/Q_c$. The inset shows $(h_c - h)/h_c$ approaches saturation as $\sqrt{(Q_c - Q)/Q_c}$. (*b*) Mean curvature κ at hump tip versus Q. The inset shows $(\kappa_c - \kappa)/\kappa_c$ approaches saturation as $\sqrt{(Q_c - Q)/Q_c}$. The dashed line depicts a square-root power law.

This suggests there exists an intermediate critical shape perturbation that neither decays nor grows upwards, but simply remains steady over time (figure 5*a*). This critical shape perturbation would correspond to an unstable hump solution.

Figure 5(*b*) illustrates the evolution of the hump curvature as a function of the flow rate for stable and unstable hump solutions. At low withdrawal flux values,

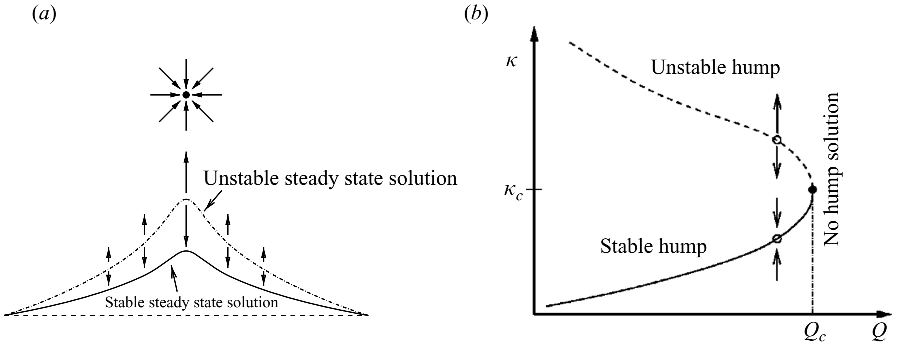

FIGURE 5. (*a*) Stable and unstable hump solutions in steady-state selective withdrawal. (*b*) Saddle-node bifurcation diagram illustrating the evolution of the hump curvature in then selective withdrawal regime.

only a very large shape perturbation can cause the interface to be drawn into the sink, we therefore expect the stable and the unstable hump shapes to be widely separated. This means the unstable hump must lie close to the sink and, as a result, has a very curved tip. At moderate withdrawal flux values, the perturbation size required to destabilize the hump solution becomes smaller, implying that the unstable and stable solutions now lie closer to each other. Concurrently, the curvature of the stable solution increases, and the curvature of the unstable solution decreases. Near transition, even a small perturbation causes the interface to become unstable and grow towards the sink. This suggests the two solutions lie very close each other and are nearly identical. Therefore it is reasonable to expect the two solutions to become identical, or coincide, at Q_c, thereby bringing about a saddle-node bifurcation of the hump solution. The square-root scaling corresponds to a smooth merging of the two solutions, so that the $\kappa(Q)$ curve at Q_c has the shape of a parabola lying on its side.

The scaling dynamics associated with how the hump solution saturates as Q approaches Q_c is consistent with a saddle-node bifurcation at Q_c. This is a generic mechanism for transition to one type of solution from another in a dynamical system with only a few degrees of freedom and suggests that the dynamics of the entire interface is coupled. However, the quantitative analysis in figure 4 shows an atypical feature: the hump height and curvature saturate towards the final scaling behaviour at very different δq values. Specifically, the square-root scaling in $h_c - h$ is evident throughout its evolution, even at large δq. In contrast, the square-root scaling for $\kappa_c - \kappa$ becomes evident only when δq has decreased below 10^{-3}. This behaviour suggests the hump shape does not approach the transition uniformly. To test this idea, we plot the hump radius at $z = h/2$ as a function of Q (figure 6). We find that the radius at the half-height saturates to the final scaling behaviour later than h, but earlier than κ as δq approaches 0. This behaviour indicates that, as Q approaches Q_c, the overall shape of the hump, e.g. the hump height or its lateral extent, saturates first, followed by features on smaller length scales. The shape of the hump at its tip, which corresponds to a feature on the smallest length scale, saturates last. This cascade of events is more typical of an approach towards a singular shape, in which features evolving on different length scales are nearly decoupled, so that features on smaller length scales saturate later than features on large length scales.

To obtain some insight into this unusual hybrid character of the interface evolution near transition, we plot κ as a function of h (figure 7). At $Q = 0$, the interface shape

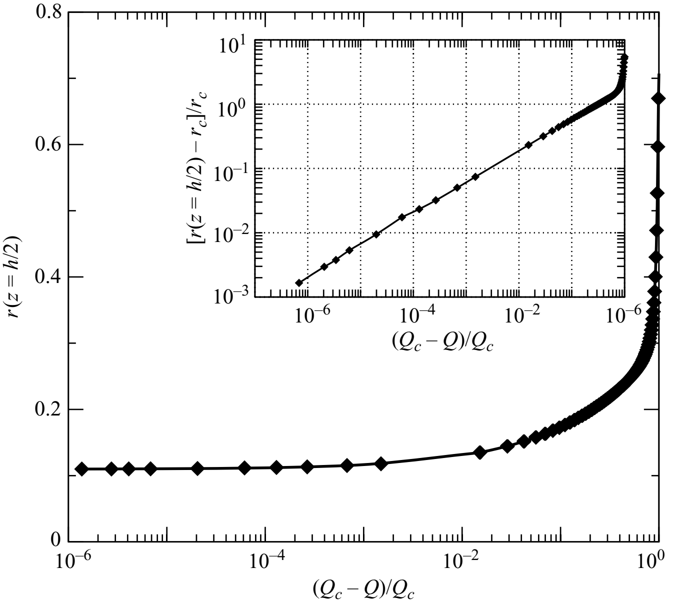

FIGURE 6. Evolution of the hump radius at $z = h/2$ as a function of $(Q_c - Q)/Q_c$. The inset shows how the radius at half-height reaches its saturation value.

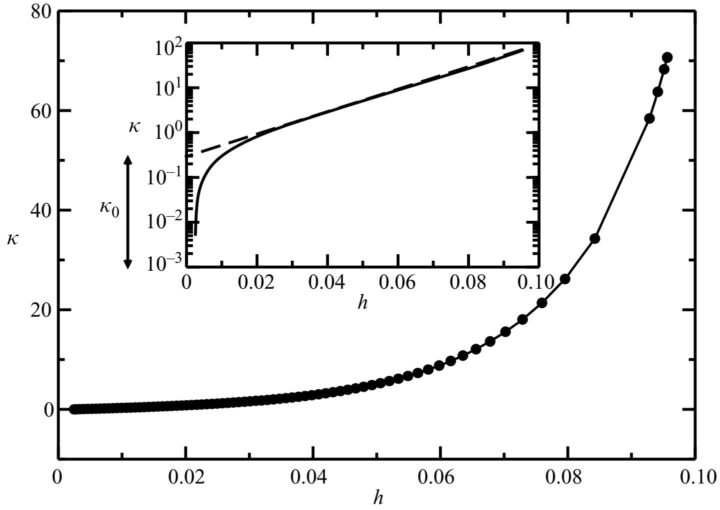

FIGURE 7. Mean curvature at the hump tip versus the hump height. Inset shows the same data on a semi-log plot. When the deflection is sufficiently large, the hump height h has a linear dependence on $\ln(\kappa)$. The dashed line indicates the logarithmic fit which intercepts $h = 0$ at κ_0.

is given by a balance of Laplace pressure and reservoir pressure p_0. For $p_0 = 0.01$, the shape is nearly a flat spherical cap. When the interface is only weakly perturbed from the $Q = 0$ shape, both κ and h increase linearly with Q, and therefore $\kappa \propto h$. This linear regime persists until $h \approx 0.02$. Beyond this point, κ increases much more rapidly than h. This large increase of κ relative to the increase in h is approximated well by a simple mathematical expression, as is evident from the inset for figure 7. In

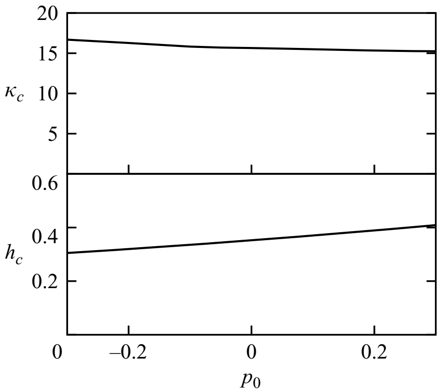

FIGURE 8. Calculated hump curvature κ_c and hump height h_c at transition as a function of the reservoir pressure p_0. The sink height $S = 1$.

the nonlinear deflection regime,

$$\ln\left(\frac{\kappa}{\kappa_0}\right) = Bh, \tag{4.2}$$

where κ_0 correspond to the intercept at $h = 0$ of the fitted line and B the slope of the logarithmic fit. This logarithmic coupling indicates that in the nonlinear regime, the hump solution evolves so that small increases in hump height correspond to large increases in the hump curvature. This does not correspond to a nearly continuous transition, as suggested by Cohen & Nagel (2002), since the hump curvature κ never decouples from the hump height. Instead, our results show that κ remains weakly coupled to h and does not diverge as the transition is approached. Logarithmic couplings are often observed near the transition between different kinds of power-law scalings as some system parameter is varied. Such logarithmic dependencies have also been shown explicitly in simple mechanics problems where the full solution can be obtained analytically (Moffatt & Duffy 1980; Dempsey 1981; Ting 1984; Dundurs & Markenscoff 1989; Barenblatt 1996). For example, the stress distribution created in a wedge by a torque being exerted at the wedge tip is described by two different types of scaling solutions, depending on the wedge opening angle. At the transition value of the opening angle, the solution develops a logarithmic dependence (Sternberg & Koiter 1958). Given these results, we may expect by analogy that the logarithmic coupling between the hump height and the hump curvature observed here could easily be perturbed by changes in the boundary conditions. In addition, it is possible that the withdrawal process analysed numerically is highly idealized and may therefore give results that are not generic. We address these concerns in §§ 4.2 and 4.3 by showing that the same evolution is obtained in a variety of withdrawal realizations.

4.2. *Interface evolution with different sink heights and reservoir pressures*

To determine the effect of the reservoir pressure p_0 on the transition structure, we analyse the numerical solutions for values of p_0 ranging from –0.3 to 0.3 with sink height $S = 1$. In figure 8 we plot κ_c and h_c, the hump curvature and hump height at transition, versus p_0. We find that the precise value of p_0 makes little difference to the values of κ_c and h_c. In addition, all the runs show the same logarithmic dependence of κ on h near the transition.

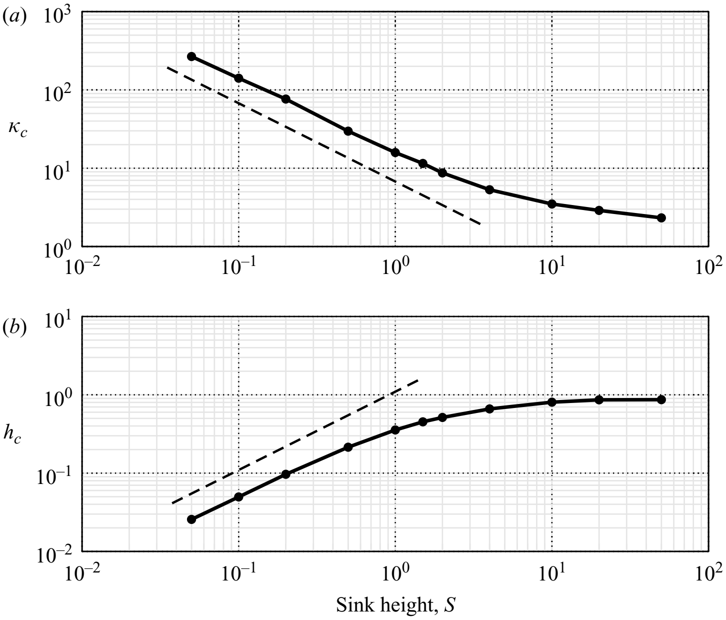

FIGURE 9. Calculated hump curvature κ_c and hump height h_c at transition with different sink heights S. The reservoir pressure $p_0 = 0.01$. The dashed line in (*a*) shows a $1/S$ dependence. The dashed line in (*b*) shows an S dependence.

In contrast, figure 9 shows that varying the sink height S strongly affects κ_c and h_c. As the dimensionless sink height S becomes much smaller than 1, or $\tilde{S} \ll a$, the hump curvature at transition, κ_c, increases as $1/S$ while h_c decreases as S. In the opposite limit, as S becomes much larger than 1, or $\tilde{S} \gg a$, both κ_c and h_c approach constant values. These trends can be understood by analysing the limiting cases where the sink is either very far from or very near to the interface. When the sink is placed very close to the interface, the effect of the pinning at a becomes irrelevant since the interface is already flat at distances $O(S)$ where the flows become very weak. Consequently, h_c and κ only depend on S when $S \ll 1$. In the opposite limit, where $\tilde{S} \gg a$, the flow at the interface becomes almost uniform because the length scale over which the imposed withdrawal flow varies is much larger than a. Under these conditions, the interface shape is primarily determined by the pinning condition at a and is insensitive to changes in the sink height.

Figure 9 also shows that the variation in κ_c tracks the variation in h_c as S is varied. Consequently, even though driving the withdrawal with a sink closer to the interface produces a larger hump curvature at transition, it does not produce a sharper hump tip. This is because the hump height, and similarly the overall deformation at transition, is proportionally smaller as well. The product $\kappa_c h_c$, which characterizes the relative separation of length scales between the hump tip and the hump height changes by a factor of about 4 when the sink height is increased by a factor of 1000, with most of the change in $\kappa_c h_c$ occurring as S becomes larger than $O(1)$. Therefore, changing the sink height primarily changes the absolute length scale of the steady-state deformation at the onset of entrainment. It does not significantly change the shape of the deformation.

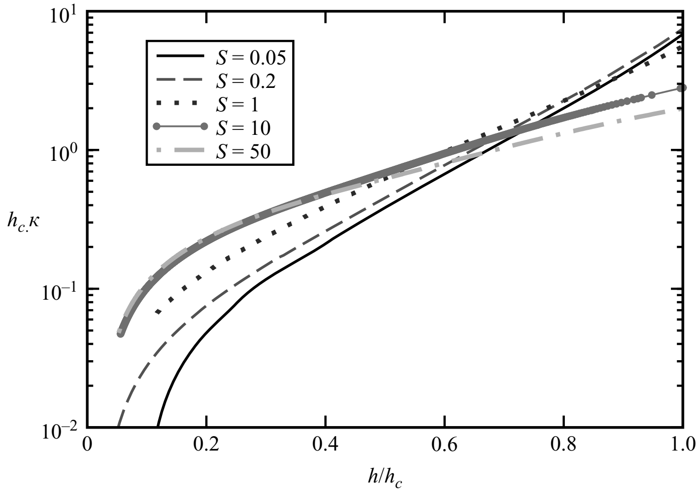

FIGURE 10. Calculated rescaled hump curvature $h_c\kappa$ versus rescaled hump height h/h_c for $S = 0.05$, 0.2, 1, 10 and 50.

This observation suggests that dividing all lengths by h_c should scale out most of the variation observed at different sink heights. In figure 10, we plot $h_c\,\kappa$ versus h/h_c obtained from numerical solutions where $S = 0.05$, 0.2, 1, 10 and 50, representing a 10^3 variation in the sink height. We find that the curves are indeed brought close together by this rescaling. We do, however, observe small changes in the slope and intercept of the logarithmic curves even when κ and h are rescaled. Nevertheless, from these results, we conclude that the logarithmic coupling is a robust feature of our idealized model of two-layer withdrawal. Changing either the boundary condition parameter p_0, or the forcing parameter S within the simple model of withdrawal produces no qualitative change in the evolution of the steady-state hump shape as a function of the withdrawal flux.

4.3. *Interface evolution under different withdrawal conditions*

Given this robustness with respect to variation in system parameters in the simple model, we next analyse the steady-state interface obtained under different realizations of selective withdrawal. In all these cases, the boundary conditions imposed on the lower-layer flow are closer approximations to realistic situations than the simplified numerical model. We find that even these different realizations, which correspond to different boundary conditions and/or imposed withdrawal flows, produce very similar steady-state hump evolutions. Figure 11 shows the interface shapes obtained in two different sets of calculations, each with a lower layer of finite depth. In the first case, the lower layer is contained in a cylindrical cell of radius a_1 and depth a_1 (figure 11*a*). This corresponds to a situation where the lower layer is confined equally in both the radial and vertical directions. The toroidal recirculation established in the lower layer is therefore much smaller in extent, thereby resulting in an $O(1)$ change in the viscous stresses exerted on the interface by the flow in the lower layer.

For this realization, the boundary-integral formulation uses a closed surface comprised of the liquid interface S_I, the sidewalls of the container S_{side} and the bottom wall of the container S_b. The disturbance velocity $\boldsymbol{u}$ on the interface is

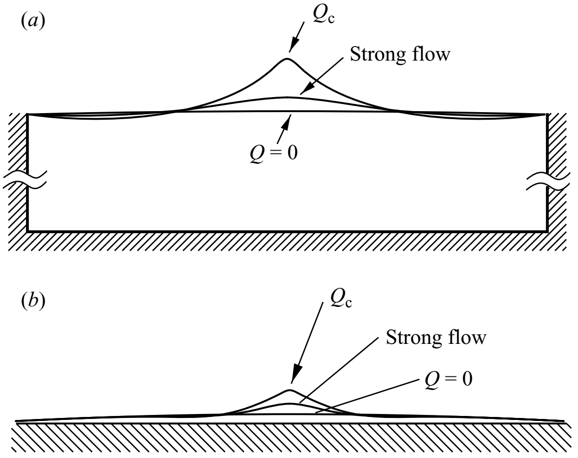

FIGURE 11. (*a*) Steady-state interface shapes obtained in selective withdrawal from a lower layer of finite depth. The cell depth is equal to the cell radius a_1 and the sink height $\tilde{S}/a_1 = 0.5$. (*b*) Steady-state interface shapes obtained in selective withdrawal from a thin lower layer overlying a solid plate of radius a_2. The sink height $\tilde{S}/a_2 = 0.2$.

given by

$$\begin{aligned}\tfrac{1}{2}\boldsymbol{u}(\boldsymbol{x}) = \int_{S_I} \boldsymbol{J}\cdot\boldsymbol{n}[\gamma 2\tilde{\kappa}]\,\mathrm{d}S_{\boldsymbol{y}} + \int_{S_{side}} \boldsymbol{J}\cdot(\boldsymbol{n}\cdot\boldsymbol{\sigma}_{(side)}\,\mathrm{d}S_{\boldsymbol{y}} \\ + \int_{S_b} \boldsymbol{J}\cdot(\boldsymbol{n}\cdot\boldsymbol{\sigma}_b)\,\mathrm{d}S_{\boldsymbol{y}} \quad \text{for } \boldsymbol{x}\in S_I,\end{aligned} \tag{4.3}$$

where $\boldsymbol{y}$ is the point on the surface that is integrated over, and $\boldsymbol{\sigma}_{side}$ and $\boldsymbol{\sigma}_b$ correspond to the normal stresses exerted by the flow on the sidewall and bottom wall of the container. The two stresses are found by solving the equation

$$\begin{aligned}\boldsymbol{0} = \int_{S_I} \boldsymbol{J}\cdot\boldsymbol{n}[\gamma 2\tilde{\kappa}]\,\mathrm{d}S_{\boldsymbol{y}} + \int_{S_{side}} \boldsymbol{J}\cdot(\boldsymbol{n}\cdot\boldsymbol{\sigma}_{side})\,\mathrm{d}S_{\boldsymbol{y}} \\ + \int_{S_b} \boldsymbol{J}\cdot(\boldsymbol{n}\cdot\boldsymbol{\sigma}_b)\,\mathrm{d}S_{\boldsymbol{y}} \quad \text{for } \boldsymbol{x}\in S_{side} \text{ or } S_b.\end{aligned} \tag{4.4}$$

This corresponds to enforcing no-slip boundary conditions on the sidewalls and the bottom walls of the container.

The interface shapes shown are the calculated results and the cell radius a_1 is used as a characteristic length scale in non-dimensionalizing various quantities. As the withdrawal flux Q and hump height increase, liquid is drawn from the lower layer into the hump. Since volume in the lower layer is conserved, gathering extra liquid into the hump forces a shallow dip in the interface shape to develop some distance away from the centreline. Thus, the hump profile no longer flattens monotonically with r, in contrast to results obtained in the simplified model. However, these slight qualitative changes to the overall shape do not significantly change how the interface evolves with Q. The shape transition still corresponds to a saddle-node bifurcation (figure 12). A comparison of the rescaled $h_c\kappa$ versus h/h_c curve obtained for a cell of finite depth and the analogous curve obtained assuming an infinitely deep layer in figure 13 show the same trend.

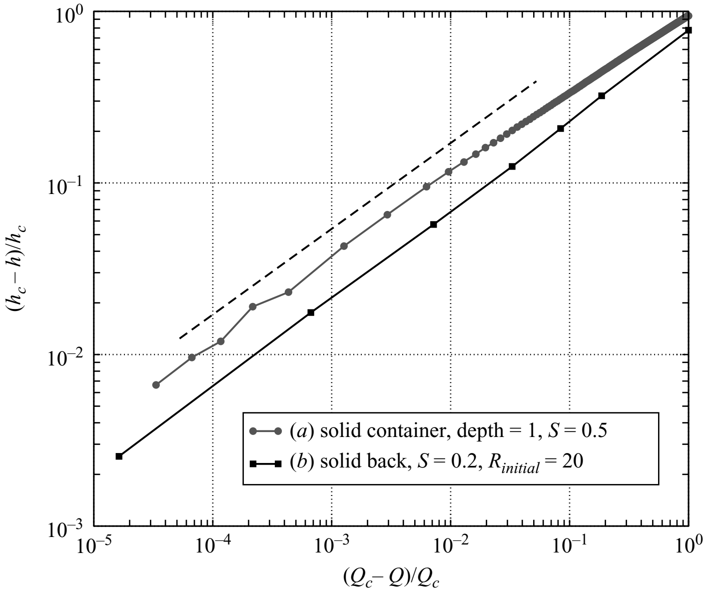

FIGURE 12. $(h_c - h)/h_c$ versus $(Q_c - Q)/Q_c$ near the transition flow rate for two-layer withdrawal. (*a*) corresponds to withdrawal from a cylindrical container. (*b*) corresponds to withdrawal from a thin lower layer which is resting on a solid plate.

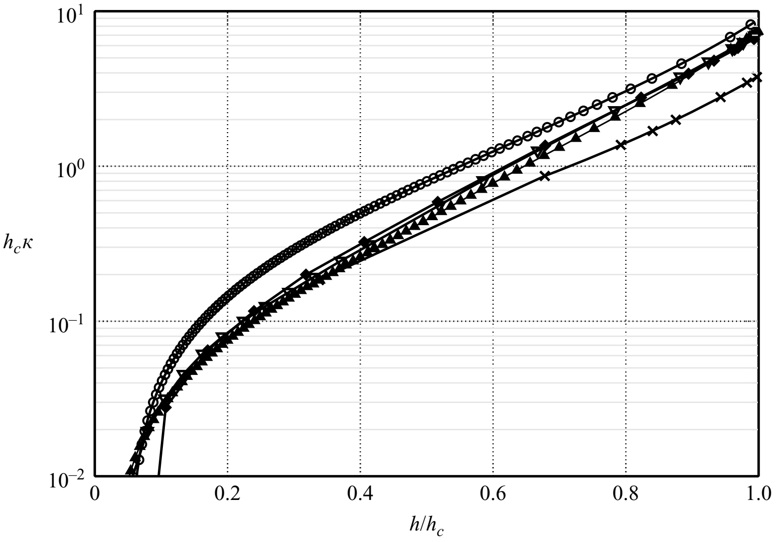

FIGURE 13. Rescaled curvature $h_c\kappa$ versus rescaled hump height h/h_c under different withdrawal conditions. Open circles correspond to withdrawal with a lower layer of finite depth contained in a cylindrical cell. The cell depth equals the cell radius a_1 and the sink height $\tilde{S}/a_1 = 0.5$. ×, withdrawal of a thin layer of liquid overlying a solid plate of radius a_2 and sink height $\tilde{S}/a_2 = 0.2$; ∇, withdrawal from a stratified layer where the capillary length scale $\ell_\gamma/a = 0.1$ and the rescaled sink height is 0.2; ◆, withdrawal driven by a vortex ring of radius $a_\omega = a$, dimensionless strength ω and height $\tilde{S}/a = 0.2$. The curve obtained for the minimal model with $S = 0.2$ and $p_0 = 0.01$ (▲) is also shown for comparison.

Figure 11(*b*) shows what happens when the condition in the lower layer is changed more drastically. In this set of calculations, a thin layer of the lower liquid overlies a solid plate. The plate radius a_2 is used as a characteristic length scale in the non-dimensionalization. The liquid is assumed to wet the solid substrate so that the plate is covered by liquid from the lower layer at all Q. The formation of a hump causes most of the liquid in the layer to drain into the hump, leaving only a very thin layer covering the rest of the solid plate. In the selective withdrawal regime, the withdrawal flow requires liquid in the lower layer to recirculate, moving along the interface towards the hump and then along the lower solid surface away from the hump. When the lower layer is thin, the viscous resistance associated with the steady-state recirculation is amplified dramatically. In this realization, the stress balance on the steady-state interface is strongly perturbed from that obtained using the simplified withdrawal model described in §§4.1 and 4.2.

For two-layer withdrawal with a thin layer of the lower liquid, the closed surface used in the boundary-integral formulation consists of the liquid interface S_I and the bottom wall of the container S_b. The equation for the velocity on the interface has the same form as (4.3) except that the terms associated with the sidewall surface S_{side} are absent. The normal stress on the solid surface $\boldsymbol{\sigma}_b$ satisfies (4.4), without the sidewall contribution.

Comparing against results from the simple model and results for withdrawal from a finite container, we can see that reducing the thickness of the lower layer has an effect on the steady-state shape of the interface obtained. The hump shape is significantly more conical, and the flattening of the interface at large r results primarily from volume conservation, rather than pinning at a_2 or the decay of the imposed withdrawal flow away from the sink. However, as is evident from figures 12 and 13, the qualitative features are unchanged. The transition still corresponds to a saddle-node bifurcation. The evolution of the hump height h retains a logarithmic coupling to the hump curvature κ. The main difference between withdrawal dynamics obtained in the simplified model and the withdrawal dynamics found for a very thin layer overlying a solid plate is a shift in the slope of the rescaled κ versus h curve.

We have also conducted a series of calculations that include the effect of hydrostatic pressure explicitly. This requires that we change the form of the normal stress jump $[\boldsymbol{n}\cdot\boldsymbol{\sigma}]_-^+$ across the liquid interface S_I in the J-integral of (3.11) and (3.13) to

$$[\gamma 2\tilde{\kappa} - \Delta\rho \boldsymbol{g}\cdot\boldsymbol{y}]\boldsymbol{n}, \tag{4.5}$$

where $\Delta\rho$ is the density difference between the two layers, $\boldsymbol{g}$ is the acceleration due to gravity and $\boldsymbol{y}$ is the location of a point on the liquid interface. Choosing the capillary length scale ℓ_γ to be less than the pinning radius a allows the interface to flatten out at large radial distances due to stratification, as occurs in the experiment, instead of due to the decay of the withdrawal flow or due to surface tension effects. Results for $\ell_\gamma/a = 0.1$ and $S = 0.2$ show that introducing stratification explicitly results in slight qualitative changes in the hump shape, but the same trend in the rescaled κ versus h curve (figure 13).

Finally, to assess the influence of details in the withdrawal flow geometry on the logarithmic coupling (4.2), we changed the imposed withdrawal flow from a sink flow (3.2), to that associated with a vortex ring of size $a_\omega = a$ and strength ω_0. The axisymmetric velocity field is given in terms of a streamfunction ϕ

$$u_r = \frac{1}{r}\frac{\partial \phi}{\partial r}, \qquad u_z = -\frac{1}{r}\frac{\partial \phi}{\partial z}, \tag{4.6}$$

and the streamfunction has the form

$$\phi(r, z) = \frac{1}{4\pi}\int\int r r' \omega(r', z')\,\mathrm{d}z'\mathrm{d}r' \int_0^{2\pi} \frac{\cos\theta\,\mathrm{d}\theta}{\sqrt{(z - z')^2 + r^2 + r'^2 - 2rr'\cos\theta}}, \tag{4.7}$$

where the vorticity distribution $\omega(r', z')$ has the form $\omega_0\delta(a_\omega - r)\delta(S - z')$ for a vortex ring. This is a better approximation of the withdrawal flow imposed in the experiment, both because there is no net volume withdrawn and because the finite size of the vortex ring mimics the finite diameter of the tube. The rescaled κ versus h curve obtained from numerical solutions for withdrawal driven by a vortex ring again has the same logarithmic coupling between the hump height and the hump curvature near the transition.

In all the different realizations of selective withdrawal, the evolution of the steady-state interface approaches the form (4.2) for large deformations. As a result, $h_c\,\kappa_c$, the relative separation of length scales characterizing the hump shape at transition, changes little even when the forcing and/or the boundary conditions are changed drastically. In other words, regardless of what type of flow we use to drive the transition, the degree of viscous resistance from flow within the lower layer, or whether the interface flattens out on large length scale due to stratification or surface tension effects, the hump shape at transition never becomes significantly sharper than that first calculated in the simple model. We conclude from this that the interface shape at Q_c produced in viscous withdrawal with two liquid layers of equal viscosity cannot be brought closer to a singular shape via changes in the boundary conditions. This contrasts sharply with theoretical results on viscous entrainment when the entrained liquid is far less viscous than the exterior, which show that interface shape at Q_c can be made singular via changes in the boundary conditions (Zhang 2004).

The robustness of the logarithmic coupling even under drastic changes in the withdrawal conditions suggests that (4.2) in fact corresponds to a generic feature of selective withdrawal from two layers of equal viscosity. This leads us to re-examine experimental measurements of κ and h, previously interpreted in terms of a continuous evolution towards a change in interface topology. In the next subsection, we compare experimental results against numerical results obtained using the simplest model of withdrawal and show that the logarithmic coupling (4.2) is also a good description of the steady-state interface evolution in the experiments.

5. Comparison with experiment

Here we compare three key results from the numerics against the measurement previously obtained by Cohen & Nagel (2002). First, we analyse the dimensional hump height $\tilde{h}(\tilde{Q})$ obtained in the experiment and show that the measurements are consistent with the interpretation that $\tilde{h}_c - \tilde{h}$ scales with $\sqrt{\tilde{Q}_c - \tilde{Q}}$ near the transition. Measurements of the hump curvature also agree well with the calculated values and begin to saturate as Q_c is approached. Finally we compare the measured κ versus h curves against the calculation and show they also agree. As a check on the validity of the simulation, we have also compared the calculated $\tilde{Q}_c(S)$ against the measured $\tilde{Q}_c(S_p)$ and found that the calculated results agree with the measurements within the experimental scatter (Case & Nagel 2005; Blanchette & Zhang 2006, 2007).

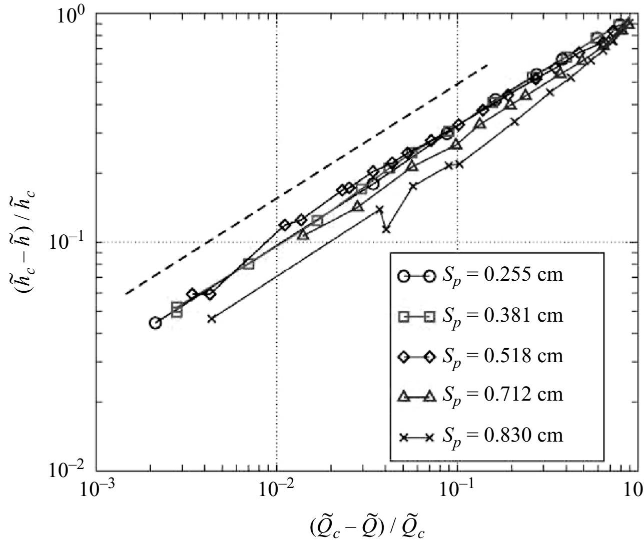

FIGURE 14. Rescaled hump heights $(\tilde{h}_c - \tilde{h})/\tilde{h}_c$ versus rescaled withdrawal flux $(\tilde{Q}_c - \tilde{Q})/\tilde{Q}_c$ for measurements obtained with five different tube heights. The capillary length scale in the experiment is 0.3 cm and the layer viscosity ratio (lower/upper) is 0.86. The calculation results are for $\tilde{S}/a = 0.2$ and reservoir pressure $p = 0.01$.

To make the comparison, we chose measurements from five different experiments, spanning the full range of tube heights used. Figure 14 shows how the measured hump height saturates as the dimensional withdrawal flux $\tilde{Q}$ approaches $\tilde{Q}_c$. As was done with the numerical results, in generating figure 14 we allowed ourselves to vary $\tilde{h}_c$ and $\tilde{Q}_c$ values within the experimental error bars, which are about 5 %, in order to generate the best power-law fits for the measurements.

For four data sets, the saturation behaviour is completely consistent with a square-root scaling. The set with the largest tube height ($S_p = 0.830$ cm) shows a slight difference in the scaling behaviour. Overall the agreement shows that the evolution of the hump height in the experiment is consistent with the existence of a saddle-node bifurcation at $\tilde{Q}_c$.

Next we compare measurements of the hump curvature against calculated values. Since the hump curvature saturates at a value of $\tilde{Q}_c - \tilde{Q}$ that is below the dynamic range of the experiment, we cannot compare the saturation dynamics directly. Instead, we compare the $\tilde{\kappa}$ curves obtained in the experiments against the results obtained using our minimal numerical model, described in § 3.1, with $S \equiv \tilde{S}/a = 0.2$ in figure 15. The same $\tilde{Q}_c$ values that produce the best power-law fit for the experimental data in figure 14 are used in figure 15. Further details about the difference between our analysis and those performed in the original papers (Cohen & Nagel 2002) can be found in the Appendix. As with the numerical results obtained for different sink heights, we account for the change in the absolute size of the hump at different tube heights by rescaling $\tilde{\kappa}$ by $\tilde{h}_c$, the dimensional hump height at transition. This causes the different curves associated with different tube heights to collapse onto roughly a single curve. Nearly all the collapsed curves show evidence of saturation as $\tilde{Q}_c - \tilde{Q}$ approaches 0. The calculated curve goes through the experimental values and shows exactly the same trend. Note that our choice of $S = 0.2$ for the numerical results is primarily a matter of simplicity, since that is the set of results discussed in § 4.1. All

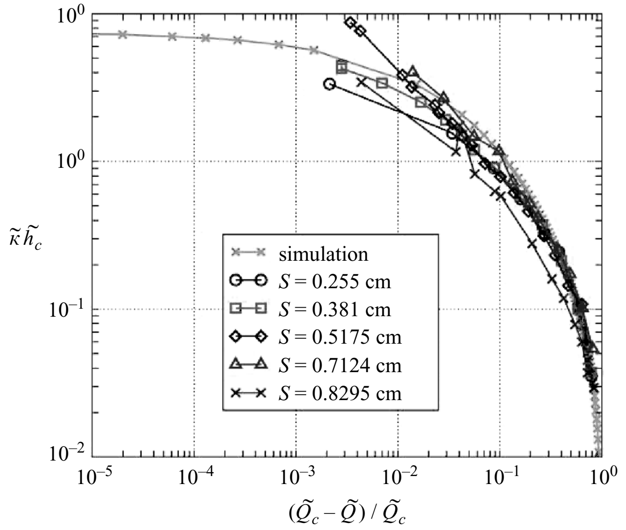

FIGURE 15. Rescaled tip curvature $\tilde{\kappa}\tilde{h}_c$ versus $(\tilde{Q}_c - \tilde{Q})/\tilde{Q}_c$ for the numerical model and experimental data. The range of the numerical results has been truncated to display the comparison clearly.

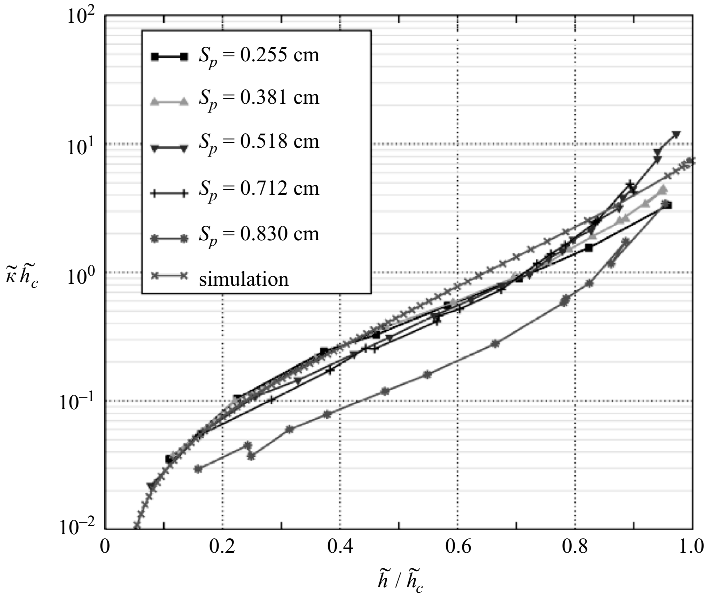

FIGURE 16. Comparison between measurements at five different pipette heights and calculation. Note the range of $\tilde{\kappa}\tilde{h}_c$ has again been truncated to display the overlap with measurements more clearly.

data corresponding to $O(1)$ values for the dimensionless sink height S show good agreement with the experiment data. From this comparison we conclude that the hump curvature also saturates in the experiment.

Finally, we plot the rescaled measured hump curvature as a function of the rescaled hump height $\tilde{h}/\tilde{h}_c$ (figure 16). The measurements at the largest tube height

($S_p = 0.830\,\mathrm{cm}$) are displaced from the other four sets. Also, the measured curves for the three larger tube heights show a slight but systematic upturn at large $\tilde{h}/\tilde{h}_c$, when compared against the calculated results. The two data sets for the lower tube heights appear to follow a logarithmic relation. Although it is unclear what causes these discrepancies, overall there is good agreement between the calculated curve and the measured curves. The agreement shows that the simple model used here captures the main features in the evolution of the steady-state interface shape.

6. Discussion and conclusion

Having shown that the results from our simple numerical model are robust under a variety of withdrawal conditions and are consistent with experimental measurements, we return to the questions that motivated our study: what is the nature of the transition from selective withdrawal to viscous entrainment? Is the surface evolution near the transition controlled by the existence of a steady-state singularity?

Figure 15 indicates that, although both the simulation and the experiments show a large increase in the hump curvature, only simulations are able to approach the transition closely enough to resolve the saturation in the hump curvature. The numerical data indicate that the maximum value of the hump curvature is finite and only a factor of 7 smaller than the hump height.

More importantly, with the numerical model, we were able to vary easily the withdrawal conditions and show explicitly that the curvature saturation value is robust against changes in the boundary conditions. In other words, the hump shape at transition cannot be brought closer to a singular shape via slight, or even significant, changes in the boundary conditions. This robustness against changes in the boundary conditions clearly shows that for equal-viscosity withdrawal, the increase in the hump curvature cannot be attributed to the existence of a singular hump solution. Instead, we find that the increase in the hump curvature is best described by a logarithmic dependence of the hump curvature on the hump height when the steady-state interface is strongly deformed. Moreover, the saturation in curvature appears much closer to transition than the saturation in the hump height. The transition is discontinuous and is analogous to simple saddle-node bifurcations in low-dimensional dynamical systems. Since the viscous stresses in the two liquid layers, and their sizes relative to surface tension effects, are not altered qualitatively when the two liquid viscosities are unequal, we expect this scenario to be the generic route by which selective withdrawal changes into viscous entrainment.

An unexpected outcome of this work is the robust logarithmic coupling between the hump curvature and the hump height for large interface deformations. We emphasize that the hump shape remains broad and well-rounded at the tip for all the flow rates, and never approaches a cylindrical shape. Therefore, the logarithmic coupling is not a result of the fact that the fundamental eigenmode for Stokes flow in cylindrical geometry is a logarithm, such as occurs in various problems where the slender-body approximation is employed.

Comparison of the surface evolution observed in equal-viscosity selective withdrawal with emulsification studies of the deformation-to-burst transition of a viscous liquid drop subjected to an axial straining flow (§ 2.6), indicate there are similarities in the qualitative trends. When the viscosity of the liquid drop is much less than the viscosity of the surrounding liquid, the curvature at the tip of the drop increases significantly with strain rate near the deformation-to-burst transition whereas the drop length saturates at a finite value. However, the surface deformations obtained in the two problems are different. In the drop emulsification problem, the drop develops a pronounced sharp tip. The radius of curvature at the tip is much smaller than the extended length of the drop. Given this large separation of length scales, it is not surprising that the behaviour of the drop curvature near transition is qualitatively different to that of the drop length. No such separation of length scale occurs in the selective withdrawal problem analysed here. The radius of curvature at the hump tip is at most a factor of 7 smaller than the hump height. Similarly, there is no obvious connection between the broad hump observed in equal-viscosity selective withdrawal and the sharp cusp-like shapes observed in the three-dimensional air drainage studies (§ 2.4).

We can also compare our results with studies of two-dimensional air entrainment (§ 2.2). In that problem, convergence towards a power-law cusp is cut off at a small length scale by the presence of finite air viscosity. In this scenario, at the limit of vanishingly small lower-layer liquid viscosity, the axisymmetric interface would approach a cusp shape at the transition from selective withdrawal to viscous entrainment. A finite, but small, lower-layer viscosity, would cause a cutoff at a length scale, whose size increases as the viscosity contrast increases. Thus, even though a singular solution is not attained for finite lower-layer viscosity, it continues to influence the surface evolution.

This scenario, however, appears to contradict existing measurements (Cohen 2004). Selective withdrawal experiments on two liquid layers of unequal viscosity have found no significant variation in the maximum hump curvature attained, even when the viscosity of the lower-layer liquid is 1000 times smaller than the viscosity of the upper-layer liquid. However, as described previously, it is difficult to resolve the maximum hump curvature accurately from experimental measurements alone since the hump curvature saturates only very close to the transition flow rate. To verify whether this proposed scenario is valid requires the available measurements to be reproduced and extended using numerical simulations of selective withdrawal at unequal viscosities.

Finally, for the sake of completeness, we mention an entirely different, and unusual scenario which may qualitatively account for the logarithmic coupling (4.2) between the curvature and the height in the steady-state interface evolution. We then show that a quantitative check allows us to rule this idea out as well. To start, we suppose there exists a singular solution for the steady-state interface at withdrawal flux Q_* significantly larger than Q_c, the withdrawal flux where a transition from selective withdrawal to viscous entrainment takes place. We also suppose that this singular hump solution is isolated, i.e. nearby values of Q do not support hump solutions. while unusual, such isolated singular solutions exist for two-dimensional selective withdrawal of inviscid fluid (Tuck & Vanden-Broeck 1984) so it is reasonable to ask whether the logarithmic coupling observed here is a manifestation of such a solution. If the singular shape occurs at $Q_* \gg Q_c$, the height of the singular hump h_* would be, correspondingly, much larger than h_c, the hump height at transition. Under these assumptions, the power-law scaling

$$\frac{\kappa}{C} = \left(\frac{h_*}{h_* - h}\right)^{\beta} \tag{6.1}$$

where C is a characteristic curvature scale, assumes an approximate logarithmic form. Since $h_c \ll h_*$, the ratio h/h_* is small over the entire range. Taylor series expansion of the natural log of (6.1) yields

$$\ln\left(\frac{\kappa}{C}\right) = -\beta \ln\left(1 - \frac{h}{h_*}\right) = \beta\left(\frac{h}{h_*} + \frac{1}{2}\left(\frac{h}{h_*}\right)^2 + \cdots\right). \tag{6.2}$$

When h_c/h_* is sufficiently small, the higher-order terms are negligible, and we obtain a logarithmic relation between κ and h

$$\ln\left(\frac{\kappa}{C}\right) = \left(\frac{\beta h_c}{h_*}\right)\frac{h}{h_c}\ . \tag{6.3}$$

According to Cohen & Nagel, the singular shape is characterized by a scaling exponent β between 0.75 and 0.82 (Cohen & Nagel 2002). In the long-wavelength analysis of spout formation, Zhang (2004) found that the steady-state spout shape approaches a singular conical shape. This would correspond to $\beta = 1$. Experimental and scaling analysis by Courrech du Pont & Eggers (2006) show that the cusp observed in a viscous drainage experiment approaches a conical shape, with $\beta = 1$. Given these values, consistency requires that the coefficient $\beta h_c/h_*$ must be much smaller than 1, since (6.3) is derived under the assumption that $h_c/h_* \ll 1$. We can check this against the numerical results by fitting the calculated κ versus h curves with the form

$$\ln\left(\frac{\kappa}{\kappa_0}\right) = b\left(\frac{h}{h_c}\right), \tag{6.4}$$

where κ_0 is the extrapolated intercept at $h = 0$ and the slope $b = \beta h_c/h_*$ in (6.3). Fits to the calculated curves for $S = 0.05$, 0.2 and 50 yield, respectively, b values 5.5, 5.9 and 1.9, all above 1. Consequently, h_c/h_* is $O(1)$ which invalidates the Taylor expansion in (6.2). This clearly rules out the possibility that the logarithmic relation reflects the existence of an isolated singular hump solution for equal-viscosity withdrawal.

7. Conclusions

In conclusion, we have created a simplified numerical model of selective withdrawal and shown that it captures the essence of the experiments. We find that the transition from selective withdrawal to viscous entrainment is discontinuous in the steady-state interface shape, and shows similar features to saddle-node bifurcations in low-dimensional dynamical systems. We also find that, when the interface is significantly deformed from the flat interface, the hump curvature has a logarithmic dependence on the hump height. We have tried to compare the selective withdrawal problem with other interface deformation problems that attribute the logarithmic coupling to the existence of a singular hump shape. None of the comparisons or proposed scenarios fully explain the logarithmic coupling seen here. Although we do not understand why the surface evolves by holding its height nearly constant and allowing its tip to become rather sharp, we have ruled out the possibility that this behaviour results from the existence of a steady-state singular hump for equal-viscosity withdrawal. Similar studies of selective withdrawal in which the fluid viscosities are varied will probably help in resolving the issues raised by our investigations.

We thank Sidney R. Nagel and Sarah Case for encouragement and helpful discussions. We also acknowledge helpful conversations with Francois Blanchette, Todd F. Dupont, Alfonso Ganan-Calvo, Leo P. Kadanoff, Robert D. Schroll, Laura Schmidt, Howard A. Stone, Thomas P. Witelski, Thomas A. Witten and Jason Wyman. This

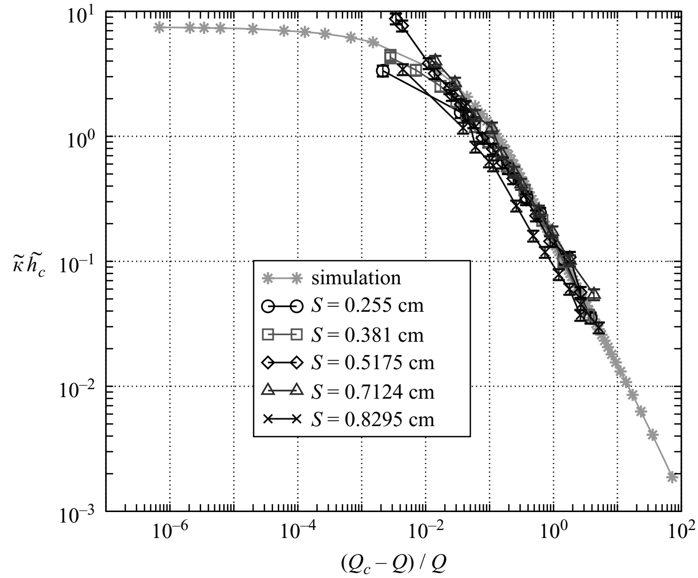

FIGURE 17. Rescaled tip curvature κh_c versus $(Q_c - Q)/Q$ for the numerical model and experimental data. The tip curvature has been non-dimensionalized using the threshold hump height h_c. Errors in the experimental tip curvature were estimated to be approximately 10 %. The model system parameters are $S = 0.2$, $p_0 = 0.01$.

research was supported by the National Science Foundation's Division of Materials Research (DMR-0213745), the University of Chicago Materials Lab (MRSEC), and by the DOE-supported ASC/Alliance Center for Astrophysical Thermonuclear Flashes at the University of Chicago.

Appendix

As was seen in previous sections, compared to the hump height, the tip curvature shows evidence of saturation towards a final value only when Q is very close to Q_c. As a consequence, when the entrainment threshold is approached, the tip curvature can appear to diverge while the hump height reaches a saturation value. In particular, when κ is plotted against $(Q_c - Q)/Q$ instead of $(Q_c - Q)/Q_c$, it is difficult to distinguish between a continued power law and a turnover into saturation with the available range of experimental data figure 17. This is because even a slight shift in the value of Q_c can straighten out the curves. The apparent power law in the $(Q_c - Q)/Q$ range between 10 and 10^{-2} seems to be an artefact of the fact that, when Q is small, the denominator of $(Q_c - Q)/Q$ is close to Q_c and almost constant, thus the entire expression scales roughly as $1/Q$. Furthermore, for small flow rates Q the system response to the outside flow can be assumed to be almost linear, with a linear dependence of κ on Q. This would then asymptotically give rise to a power law with an exponent of -1. We also note that the Q_c values quoted here for the measurements have been adjusted within the measurement error to give the best fit to the saddle-node scaling. In the previous experimental papers (Cohen & Nagel 2002; Cohen 2004), the measurements had been analysed assuming that the hump curvature diverges at Q_c. This previous definition of Q_c corresponds to what we call Q_*. The important point is that, in both cases, the size of the adjustment in Q_c is small, within the error bar, and comparable in size.

REFERENCES

Acrivos, A. & Lo, T. S. 1978 Deformation and breakup of a single slender drop in an extensional flow. *J. Fluid Mech.* **86**, 641–672.

Anna, S. L., Bontourx, N. & Stone, H. A. 2003 Formation of dispersions using flow focusing in microchannels. *Appl. Phys. Lett.* **82**, 364–366.

Barenblatt, G. I. 1996 *Scaling, Self-Similarity, and Intermediate Asymptotics*. Cambridge University Press.

Blanchette, F. & Zhang, W. W. 2006 Transition flow rate in viscous withdrawal. APS-DFD Meeting, OJ006B.

Blanchette, F. & Zhang, W. W. 2007 Selective withdrawal in liquids of uneven viscosities. Preprint.

Blawzdziewicz, J., Cristini, V. & Loewenberg, M. 2002 Critical behavior of drops in linear flows. I. Phenomenological theory for drop dynamics near critical stationary states. *Phys. Fluids* **14**(8), 2709–2718.

Buckmaster, J. D. 1973 The bursting of pointed drops in slow viscous flow. *J. Appl. Mech.* E **40**, 18–24.

Case, S. & Nagel, S. R. 2005 Selective withdrawal with an inverted viscosity ratio. *APS March Meeting*, H37.008.

Case, S. C. & Nagel, S. R. 2007 Spout states in the selective withdrawal of immiscible fluids through a nozzle suspended above a two-fluid interface. *Phys. Rev. Lett.* **98**, 114501.

Chaieb, S. 2004 Free surface deformation and cusp formation during the drainage of a very viscous fluid. ArXiv:physics/0404088.

Cohen, I. 2004 Scaling and transition structure dependence on the fluid viscosity ratio in the selective withdrawal transition. *Phys. Rev.* E **70**, 026302.

Cohen, I. & Nagel, S. 2002 Scaling at the selective withdrawal transition through a tube suspended above the fluid surface. *Phys. Rev. Lett.* **88** (7), 074501.

Cohen, I., Brenner, M. P., Eggers, J. & Nagel, S. R. 1999 Two fluid snap-off problem: experiments and theory. *Phys. Rev. Lett.* **83**(6), 1147–1150.

Cohen, I., Li, H., Hougland, J. L., Mrksich, M. & Nagel, S. R. 2001 Using selective withdrawal to coat microparticles. *Science* **292**, 265–267.

Courrech du Pont, S. & Eggers, J. 2006 Tip singularity on a liquid–gas interface. *Phys. Rev. Lett.* **96**, 034501.

Davaille, A. 1999 Simultaneous generation of hotspots and superswells by convection in a heterogenous planetary mantle. *Nature* **402**, 756–760.

Dempsey, J. P. 1981 The wedge subjected to tractions: a paradox resolved. *J. Elasticity* **11**, 1–10.

Doshi, P., Cohen, I., Zhang, W. W., Siegel, M., Howell, P., Basaran, O. A. & Nagel, S. R. 2003 Persistence of memory in drop breakup: the breakdown of universality. *Science* **302**, 1185–1188.

Dundurs, J. & Markenscoff, X. 1989 The Sternberg–Koifer conclusion and other anomalies of the concentrated couple. *Trans. ASME* E: *J. Appl. Mech.* **56**, 240–245.

Eggers, J. 1997 Nonlinear dynamics and breakup of free-surface flows. *Rev. Mod. Phys.* **69**, 865–929.

Eggers, J. 2001 Air entrainment through free-surface cusps. *Phys. Rev. Lett.* **86** (19), 4290–4293.

Eggers, J., Lister, J. R. & Stone, H. A. 1999 Coalescence of liquid drops. *J. Fluid Mech.* **401**, 293–310.

Forbes, L. K., Hocking, G. C. & Wotherspoon, S. 2004 Salt-water up-coning during extraction of fresh water from a tropical island. *J. Engng Maths* **48**, 69–91.

Grace, P. 1982 Dispersion phenomena in high viscosity immiscible fluid systems and application of static mixers as dispersion devices in such systems. *Chem. Engng Commun.* **14**, 225–239.

Hocking, G. C. & Forbes, L. K. 2001 Super-critical withdrawal from a two-layer fluid through a line sink if the lower layer is of finite depth. *J. Fluid Mech.* **428**, 333–348.

Imberger, J. & Hamblin, P. F. 1982 Dynamics of lakes, reservoirs and cooling ponds. *Annu. Rev. Fluid Mech.* **14**, 153–187.

Ivey, G. N. & Blake, S. 1985 Axisymmetrical withdrawal and inflow in a density-stratified container. *J. Fluid Mech.* **161**, 115–137.

Jellinek, A. M. & Manga, M. 2002 The influence of a chemical boundary layer on the fixity, spacing and lifetime of mantle plumes. *Nature* **418**, 760–763.

Jeong, J.-T. & Moffatt, H. K. 1992 Free-surface cusps associated with flow at low Reynolds number. *J. Fluid Mech.* **241**, 1–22.

Joseph, D. D., Nelson, J., Renardy, M. & Renardy, Y. 1991 Two-dimensional cusped interfaces. *J. Fluid. Mech.* **223**, 383–409.

Ladyzhenskaya, O. A. 1963 *The Mathematical Theory of Viscous Incompressible Flow*. Gordon and Breach.

Lee, S. H. & Leal, L. G. 1982 The motion of a sphere in the presence of a deformable interface. II. A numerical study of the translation of a sphere normal to an interface. *J. Colloid Interface Sci.* **87**, 81–106.

Limat, L. & Stone, H. 2004 Three-dimensional lubrication model of a contact line corner singularity. *Europhys. Lett.* **65**, 365–371.

Link, D. R., Anna, S. L., Weitz, D. A. & Stone, H. A. 2004 Geometrically mediated breakup of drops in microfluidic devices. *Phys. Rev. Lett.* **92**, 054503.

Lister, J. R. 1989 Selective withdrawal from a viscous two-layer system. *J. Fluid Mech.* **198**, 231–254.

Lorenceau, E., Restagno, F. & Quéré, D. 2003 Fracture of a viscous liquid. *Phys. Rev. Lett.* **90** (184501).

Lorenceau, E., Quéré, D. & Eggers, J. 2004 Air entrainment by a viscous jet plunging into a bath. *Phys. Rev. Lett.* **93**, 254501.

Lorenceau, E., Utada, A. S., Link, D. R., Cristobal, G., Joanicot, M. & Weitz, D. A. 2005 Generation of polymerosomes from double-emulsions. *Langmuir* **21**, 9183–9186.

Lorentz, H. A. 1907 Ein allgemeiner satz, die bewegung einer reibenden flüssigkeit betreffend, nebst einigen anwendungen. *Abh. üb. theor. Physik* **1**, 23.

Lubin, B. T. & Springer, G. S. 1967 The formation of a dip on the surface of a liquid draining from a tank. *J. Fluid Mech.* **29**, 385–389.

Miloh, T. & Tyvand, P. A. 1993 Nonlinear transient free-surface flow and dip formation due to a point sink. *Phys. Fluids* A **5**, 1368–1375.

Moffatt, H. K. & Duffy, B. R. 1980 Local similarity solutions and their limitations. *J. Fluid Mech.* **96**, 299–313.

Navot, Y. 1999 Critical behavior of drop breakup in axisymmetric viscous flow. *Phys. Fluids* **11**, 990–996.

Oddershede, L. & Nagel, S. R. 2000 Singularity during the onset of an electrohydrodynamic spout. *Phys. Rev. Lett.* **85**.

Oguz, H. N. & Prosperetti, A. 1990 Bubble entrainment by the impact of drops on liquid surfaces. *J. Fluid Mech.* **219**, 143–179.

Pozrikidis, C. 1992 *Boundary Integral and Singularity Methods for Linearized Viscous Flow*. Cambridge University Press.

Rallison, J. M. & Acrivos, A. 1978 A numerical study of the deformation and burst of a viscous drop in an extensional flow. *J. Fluid Mech.* **89**, 191–200.

Renardy, M. & Renardy, Y. 1985 Perturbation analysis of steady and oscillatory onset in a Bénard problem with two similar liquids. *Phys. Fluids* **28**, 2699–2708.

Renardy, Y. & Joseph, D. D. 1985 Oscillatory instability in a Bénard problem of two fluids. *Phys. Fluids* **28**, 788–793.

Sautreaux, C. 1901 Mouvement d'un liquide parfait soumis à lapesaneur. Détermination des lignes de courant. *J. Math. Pures Appl.* **7**, 125–159.

Simpkins, P. & Kuck, V. J. 2000 Air entrapment in coatings by way of a tip-streaming meniscus. *Nature* **403**, 641–643.

Sternberg, E. & Koiter, W. T. 1958 The wedge under a concentrated couple: a paradox in the two-dimensional theory of elasticity. *Trans. ASME* E: *J. Appl. Mech.* **25**, 575–81.

Stokes, T. E., Hocking, G. C. & Forbes, L. K. 2005 Unsteady flow induced by a withdrawal point beneath a free surface. *Anziam J.* **47**, 185–202.

Stone, H. A. 1994 Dynamics of drop deformation and breakup in viscous fluids. *Annu. Rev. Fluid Mech.* **65**, 65–102.

Taylor, G. I. 1934 The formation of emulsions in definable fields of flow. *Proc. R. Soc.* A **146**, 501–523.

Taylor, G. I. 1964 Conical free surfaces and fluid interfaces. *Proc. 11th Intl Cong. Appl. Mech.* pp. 790–796.

Thoroddsen, S. T., Takehara, K. & Etoh, T. G. 2005 The coalescence speed of a pendant and a sessile drop. *J. Fluid Mech.* **527**, 85–114.

Ting, T. C. T. 1984 The wedge subjected to tractions: a paradox re-examined. *J. Elasticity* **14**, 235–47.

Tuck, E. O. & Vanden-Broeck, J.-M. 1984 A cusp-like free-surface flow due to a submerged source or sink. *J. Austral. Math. Soc.* B **25**, 443–450.

Utada, A. S., Lorenceau, E., Link, D. R., Kaplan, P. D., Stone, H. A. & Weitz, D. A. 2005 Monodisperse double emulsions generated from a microcapillary device. *Science* **308**, 537–541.

Vanden-Broeck, J.-M. & Keller, J. B. 1987 Free surface flow due to a sink. *J. Fluid Mech.* **175**, 109–117.

Wyman, J., Dillmore, S., Murphy, W., Garfinkel, M., Mrksich, M. & Nagel, S. R. 2004 Microencapsulation of Islets of Langerhans via selective withdrawal to achieve immunoisolation. *APS March Meeting*, W9.008.

Zhang, W. W. 2004 Viscous entrainment from a nozzle: singular liquid spouts. *Phys. Rev. Lett.* p. 184502.

Zhang, W. W. & Lister, J. R. 1999 Similarity solutions for capillary pinch-off in fluids of differing viscosity. *Phys. Rev. Lett.* **83**, 1151–1154.